The Rovibronic Analysis of the Optical Spectra of Transition Metal Complexes

By

Thomas W. Hayes

A DISSERTATION PRESENTED TO THE GRADUATE SCHOOL
OF THE UNIVERSITY OF FLORIDA IN PARTIAL FULFILLMENT
OF THE REQUIREMENTS FOR THE DEGREE OF
DOCTOR OF PHILOSOPHY

UNIVERSITY OF FLORIDA

1997

This dissertation is dedicated to the memory of my father, whose support and encouragement will never be forgotten.

ACKNOWLEDGMENTS

The analysis of the data presented in this dissertation would not have been possible without the guidance of my mentor Phil Brucat. I feel honored to have had the opportunity to benefit from his knowledge and expertise. I must also thank my fellow group members and good friends Darrin Bellert and Thandi Buthelezi for their aid over the course of my graduate studies. I have enjoyed our many discussions and have benefitted from them immensely.

TABLE OF CONTENTS

ACKNOWLEDGMENTS iii

LIST OF TABLES vi

LIST OF FIGURES viii

Abstract x

1 INTRODUCTION 1

2 EXPERIMENT 6
Experimental Apparatus and Overview 6
Methods of Photodissociation 10
One-Color Experiments 10
Two-Color Experiments 12
Calibration of Mass Spectra 12
Calibration of Photodissociation Spectra 15

3 SIMULATION OF ROTATIONAL SPECTRA 21
Rotational Energy Levels 21
Effect of Total Angular Momentum 23
Effect of Temperature 27
Rotational Spectrum Simulator 28
Fitting Procedure 29
Errors in Rotational Constants and Bond Lengths . . 33

4 PHOTODISSOCIATION OF GROUP VB METAL-RARE GAS CATIONS . 36
Vibrational Structure of Electronic Spectra 39
Vibrational Analysis of Electronic Spectra 40
Determination of Dissociation Energies 66
Rotational Analysis of VAr^+ and $NbAr^+$ 74
Parameterization of VAr^+ B-State Potential Energy Surface 83
Qualitative Trends in the Photodissociation Spectra 95
Trends in Binding Energy 98
Comparison to Theoretical Calculations 100
Conclusions 102

5 THE PHOTODISSOCIATION OF $V^+ \cdot CH_4$ 104
Vibrational analysis 105
Discussion 111
Conclusions 114

6 THE BOND LENGTH OF CoO^+ 116
Rotational Analysis 117
Discussion 121
Summary 123

APPENDIX 124
TOFMS Program Description 124
TOFMS.C Program Code 126
1K Program Description 135
1K.c Program Code 138

LIST OF REFERENCES 157

BIOGRAPHICAL SKETCH 162

LIST OF TABLES

Table

2-1. Laser Dye Ranges and Peak Outputs 9

4-1. Spectroscopic Constants of VAr^+ 49

4-2. Spectroscopic Constants of $NbAr^+$ 50

4-3. Spectroscopic Constants of $TaAr^+$ 50

4-4. Spectroscopic Constants of VKr^+ 51

4-5. Spectroscopic Constants of VXe^+ 51

4-6. Spectroscopic Constants of $NbXe^+$ 51

4-7. Line Positions of the VAr^+ Excited States . . . 52

4-8. Line Positions of the $NbAr^+$ Excited States . . 53

4-9. Line Positions of the $TaAr^+$ Excited States . . 54

4-10. Line Positions of the VKr^+ Excited States . . . 55

4-11. Band Positions in the VXe^+ A-X System 56

4-12. Band Positions in the $NbXe^+$ A-X System 57

4-13. Rotational Constants of the B-State of VAr^+ . . 79

4-14. Bond Lengths and Dissociation Energies of Selected M^+-Ar Complexes 83

4-15. Comparison of Morse Functions for the $^5\Pi_1$ B State of VAr^+ 87

4-16. Parameters of and Constants Calculated from the Born-Mayer Potential of the B-State of VAr^+ . . 94

4-17. Selected Experimental Binding Energies of

Group VB Rare Gas Cations 99

4-18. Ground State Dissociation Energies of Selected Transition Metal Cation-Argon Complexes 101

5-1. Frequencies of Assigned Transitions in $V^+ \cdot CH_4$ in (cm^{-1}) 110

5-2. Molecular constants of $V^+ \cdot CH_4$ (cm^{-1}) 111

5-3. First-Row ground state $M^+ \cdot CH_4$ binding energies 114

6-1. Transition Frequencies and Rotational Constants of the A-State of CoO^+ 119

6-2. Spectroscopic Constants of CoO^+ 121

6-3. Selected Spectrometric Parameters of CoO^+, CoO, and FeO 122

A-1. Commands Supported by Program TOFMS 125

A-2. Commands Supported by Program 1K 136

LIST OF FIGURES

2-1. Schematic of the Experimental Apparatus 7

2-2. Time-of-Flight Mass Spectrum of VAr^+ 16

2-3. Time-of-Flight Mass Spectrum of $NbKr^+$ 17

2-4. Neon Optogalvanic Transitions 20

3-1. Relationship Between Band Degradation and (B'-B'') 24

3-2. Effect Of Ω'' On Branch Structure. 25

3-3. Effect of ΔΩ On The Branch Intensities. 26

3-4. Screen Dump of Rotational Simulator. 31

3-5. Determination of (B'-B'') From Branch Structure.35

4-1. Photodissociation Spectrum of VAr^+ 41

4-2. Photodissociation Spectrum of $NbAr^+$ 42

4-3. Photodissociation Spectrum of $TaAr^+$ 43

4-4. Photodissociation Spectrum of VKr^+ 44

4-5. Photodissociation Spectrum of $NbXe^+$ 45

4-6. Photodissociation Spectrum of VXe^+ 46

4-7. Morse Fits of the Excited States of VAr^+ . . . 58

4-8. Morse Fits of the Excited States of $NbAr^+$ . . . 59

4-9. Morse Fits of the Excited States of $TaAr^+$ . . . 60

4-10. Morse Fits of the Excited States of VKr^+ . . . 61

4-11. Morse Fits of the Excited States of VXe^+ . . . 62

4-12. Morse Fits of the Excited States of $NbXe^+$ . . . 63

4-13. Assignment of VKr^+ Vibrational Numbering Through Isotopic Shifts 64

4-14. Assignment of $NbXe^+$ Vibrational Numbering Through Isotopic Shifts 65

4-15. Leroy-Bernstein Extrapolations of V^+-Rare Gas Cations 68

4-16. Leroy-Bernstein Extrapolations of Nb^+-Rare Gas Cations 69

4-17. Leroy-Bernstein Extrapolations of $TaAr^+$ 70

4-18. Rotational Structure in the B-X System of VAr^+ 76

4-19. Vibrational Dependence of B-X VAr^+ Rotational Constants 78

4-20. Molecular Orbital Diagram of the Ground State of VAr^+ 81

4-21. Rotational Fit of the (4,0) a-X Transition in $NbAr^+$ 82

4-22. Born-Mayer Potential of the B-State of VAr^+ . . 90

4-23. Comparison of the Vibrational Energy Levels Predicted by the Morse and Level BM[exp,4,6] Fits to Experimental Transition Frequencies 92

4-24. Comparison of the Level BM[exp,4,6] Rotational Constants to Experiment 93

4-25. Correlation Diagram of the Group VB Atomic Energy Levels 97

5-1. Photodissociation Spectrum of VCH_4^+ 107

5-2. Fit of VCH_4^+ Band Positions 108

6-1. Fit to the (0,2) Band of the A-State of CoO^+. 118

6-2. Vibrational Dependence of the A-State Rotational Constants. 120

Abstract of Dissertation Presented to the Graduate School of the University of Florida in Partial Fulfillment of the Requirements for the Degree of Doctor of Philosophy

THE ROVIBRONIC ANALYSIS OF THE OPTICAL SPECTRA OF TRANSITION METAL COMPLEXES

By

Thomas W. Hayes

December, 1997

Chairperson: Philip J. Brucat
Major Department: Chemistry

High resolution photodissociation spectroscopy has been utilized to probe the rovibronic transitions of group VB transition metal mono-cations electrostatically bound to Ar, Kr, Xe and CH_4. The cationic complexes have been generated via a laser driven supersonic-expansion source and isolated using a custom time-of-flight mass spectrometer prior to interrogation with the visible output of a tunable Nd^{3+}:YAG pumped dye laser. The vibrational and rotational analysis of the action spectra yield the spectroscopic constants of the excited state involved in the optical transition. In many instances, accurate assignments of the atomic asymptotes into which the complexes dissociate have been

made, allowing ground state binding energies to be extracted via a Leroy-Bernstein extrapolation. The ground and excited state binding energies have been found to be dependent upon both the electron configuration of the metal cation and the polarizability of the ligand.

In addition, the rotational analysis of covalently bound CoO^+ is presented. The rotational constants, ground and excited state bond lengths, and vibration-rotation coupling constant of the single excited state observed are reported. The rotational structure is assigned to a perpendicular transition from a ground state with $^5\Delta_i$ symmetry.

CHAPTER 1
INTRODUCTION

The intricate natures of the different forces which comprise chemical bonds have been the subject of numerous studies pursued quite vigorously for a number of years. From the onset, it was understood that research which focused on the smaller, more tractable diatomics would aid in the understanding of more complex polyatomic species. A pioneer of this work, Gerhard Herzberg, dedicated much of his life to summarizing these early findings into "Spectra of Diatomic Molecules" [1] which has become a valuable tool and primer for any researcher in this continually expanding research area. The majority of molecules studied at this time were simple covalent species, important, but just a single representative of the diversity present in chemical systems. The covalent bond, although critical to the understanding of intra-molecular bonding, does not explain the dynamics of reactions in solution, nor even the interactions between the species comprising the solution itself. These solvent based interactions are extremely important and are even today relatively unexplored

frontiers.

The first step toward categorizing any new system, as pointed out earlier, is the study of simple prototypes. The simplest model of solvation would be that of a single solute interacting with just one solvent species. It is of course advantageous to select a solute/solvent pair which is but one member of a larger set, whose members share a common bonding mechanism and are capable of being probed by similar experimental techniques. We have chosen to study the charge-(induced dipole) association present between transition metal cations and various closed shell ligands. $Metal^+$-Ligand (ML^+) Charge-(induced dipole) associations are not only important to the understanding of solvation but, by virtue of the high density of low-lying atomic energy levels resident upon a transition metal cation, lend themselves to probing by visible spectroscopic techniques.

A ML^+ charge-(induced dipole) attraction may be easily understood from simple electrostatics [2]. The metal cation may be viewed as a point charge, q, which distorts the electron cloud of a closed shell neutral species resulting in an induced dipole. The ability of the ligand to be distorted is reflected by the magnitude of its polarizability, α, and the attractive force, negative by convention, is a function of both the polarizability and the internuclear separation, r, as shown in Equation 1-1.

$$U(r) = \frac{-q^2\alpha}{2r^4} \qquad (1\text{-}1)$$

In this study the ML^+ charge-(induced dipole) attraction is probed by high-resolution photodissociation spectroscopy in combination with molecular beam and time-of-flight (TOF) mass spectrometric techniques. The ions are formed through the use of a supersonic expansion [3] which creates cluster ions with an absolute minimum of internal energy. The "cold" ion ensemble reduces the number of electronic transitions to those which originate from the vibrationless level of the ground state, vastly simplifying the analysis of the resulting spectra. Mass selection using a TOF mass spectrometer allows for a single parent ion to be isolated and then optically interrogated without contamination by other ML^+ complexes which may have been present in the nascent ion ensemble. Finally, modern dye lasers have both sufficient power and resolution to probe the rovibronic transitions accessible in the visible region of the spectrum. By restriction of laser frequency to the visible region, the energy levels of the closed shell ligands are not accessible and therefore transitions are centralized on the metal cation.

The astute reader will now realize one obvious

limitation of this technique. Through limiting the origin of the transition to a single vibrational level of the ground state, only excited state information may be obtained. This is not rigorously true. In certain cases the excited state potentials are so well understood that accurate ground state information, including binding energies [4,5,6,7] and bond lengths [8,9,10], can be extracted from the excited state analysis. The means by and conditions under which this is accomplished are outlined within Chapter 4 of this manuscript.

The majority of this dissertation deals with the analysis of the rovibronic spectra obtained for the Group VB transition metal cations (M^+ = vanadium, niobium or tantalum) bound to the noble monotonic ligands argon, krypton or xenon. This investigation has yielded both ground and excited state spectroscopic constants including vibrational frequencies, anharmonicities, binding energies and in some cases bond lengths. From this data trends have been identified which relate our findings to the electronic structure of the transition metal cations. In two cases, VAr^+ and $NbAr^+$, sufficient information is available to parameterize different analytic potential energy functions and evaluate how well they describe the excited state surface.

After discussing the Group VB metal cationic complexes

formed from the noble gases, the analysis of the resonant photodissociation spectrum of V^+CH_4 will be presented. Methane is an example of a closed shell polyatomic ligand that has been found to behave very similarly to the rare gas ligands. In addition to observing an excited state progression in the stretching mode, a rocking mode built upon the stretch has been observed. Insight into the structure of the complex has been obtained from comparison of the spectroscopic constants obtained with theoretical calculations.

Finally, the rotational analysis of CoO^+ will be presented. This departure from the charge-(induced dipole) associations mentioned thus far shows the applicability of the photodissociation technique to covalently bound complexes.

CHAPTER 2
EXPERIMENT

Experimental Apparatus and Overview

Figure 2-1 displays a representation of the experimental apparatus used in acquiring photodissociation spectra. The formation of atomic and cluster ions is achieved through the use of a laser-driven-plasma supersonic-expansion source utilizing the second harmonic of a pulsed Nd^{+3}:YAG laser for ignition. The vaporization laser (7 ns duration, ~15 mJ/pulse) is focused upon a rotating rod of the metal of interest resulting in a plasma. The firing of the dissociation laser is timed to coincide with the opening of a pulsed valve (open for 100-200 μs) which admits helium seeded with <1% of the ligand (L) of interest at a backing pressure of 50-120 psi. The He/L mixture serves as a carrier gas for the expansion of the plasma and allows for the complexation and cooling of ML^+ ions. The ions are collimated by passage through two conical skimmers and the three regions of the vacuum chamber thus defined are differentially pumped to yield an ultimate pressure at the entrance of the mass spectrometer

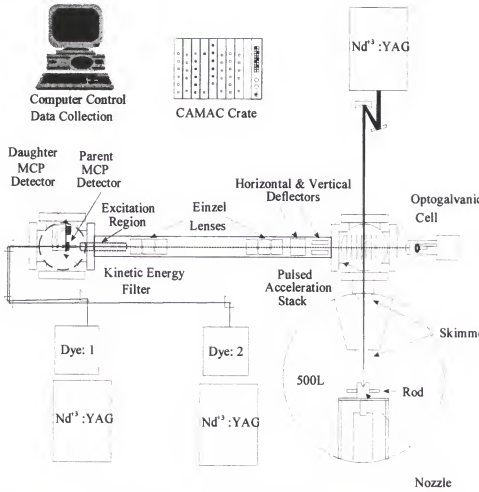

Figure 2-1. Schematic of the Experimental Apparatus.

The experiment is initiated by the firing of the vaporization laser (top right) which triggers the opening of the pulsed valve (seated behind the target rod) and the formation of the supersonic expansion. The complexes thus formed are collimated by two skimmers and injected 90 degree off the neutral beam axis and into a custom time of flight mass spectrometer. The ions are accelerated to ca. 1.45 keV down the flight tube where they are centered and focused by deflectors and Einzel lenses. In the one-color photodissociation experiment, the first dye laser is fired when the parent ion of interest is in the excitation region of the apparatus. When a two-color experiment is desired the second laser is fired after the first, promoting the complexes in the excited state prepared by the first laser pulse above the adiabatic dissociation limit. Photodissociation spectra are acquired by monitoring daughter ion photocurrent. Neon optogalvanic transitions acquired simultaneously with unknown action spectra allow for accurate calibration.

on the order of $1x10^{-7}$ torr. Here the positive ions are turned 90° out of the neutral molecular beam and accelerated to c.a. 1.45 keV down the 2.5 m flight tube of a custom TOF mass spectrometer. A series of electrostatic optics guide the ions through the flight-tube and into a 180° electrostatic sector which serves as a kinetic energy filter. Mass spectra of the cationic complexes produced in the plasma can be obtained by setting the kinetic energy filter to transmit ions which have the full kinetic energy of the beam.

Photoexcitation of the ML^+ is accomplished prior to entrance into the electrostatic sector by a tunable Nd^{+3}:YAG pumped dye laser. In the two-color experiment the second dye laser (dump laser) is fixed at a non-resonant frequency and fired after the first (pump laser), promoting the complexes in the excited state prepared by the first laser above the adiabatic dissociation limit. The time delay between the pump and dump laser varies with the excited state lifetime. The laser dyes used in the region from 11400-18200 cm^{-1}, and the maximum output of each with an 80 mJ Nd^{+3}:YAG second harmonic pump, are listed in Table 2-1. The metal ions produced as photofragments of the mass selected ion complex are observed at the arrival time of the precursor ion but with the approximate kinetic energy of the parent ion multiplied by the ratio of the fragment to parent

Table 2-1. Laser Dye Ranges and Peak Outputs

Dye	Range of Use (cm^{-1})	Peak Output (mJ/pulse)
LDS 867	11400-11800	15
LDS 821	11800-12600	20
LDS 768	12600-13200	25
LD 700	13200-14000	30
LD 698	13800-14900	35
DCM II	14900-16000	35
R640	16000-16500	30
R640/R610 mix	16500-16900	30
R610	16800-17000	25
R610/R590 mix	17000-17200	30
R590	17200-18200	35

ion mass. The configuration of the mass spectrometer used in this study limits parent mass resolution to one part in 200 and secondary mass resolution to one part in ten.

The entire experimental sequence of ion formation, mass selection, photoexcitation, and detection is pulsed and repeated at 9.1 Hz. Sixteen experimental cycles are accumulated and averaged for every optical resolution element of the spectrum. Typically vibrational spectra are acquired at 0.15 cm^{-1}/s while rotational spectra are scanned more slowly at 0.01cm^{-1}/s. A CAMAC crate/microcomputer data station operating with real-time software provides for

system control and data acquisition. The resultant photodissociation spectrum is calibrated through the use of neon optogalvanic transitions which are acquired simultaneously with unknown photodissociation spectra. Finally, the action spectrum is Doppler shift corrected for the laboratory velocity of the parent ion.

Methods of Photodissociation

The photodissociation spectra presented in this dissertation originate from two different approaches. Chapters 4 and 5 contain spectra which were obtained from absorption of a single photon leading to a rapid predissociative event. If an excited state does not couple effectively to a dissociation process, as is the case in Chapter 6 where CoO^+ is presented, a second non-resonant photon may be used. The second photon excites the level prepared by the first laser to a second excited state which may predissociate. The first laser which prepares the initial excited state is referred to as the "pump" laser while the second is called the "dump" laser.

One-Color Experiments

One-color photodissociation is the most common method

implemented in our experimental procedure. The most critical element is overlapping the dissociation laser with the parent ion packet as it traverses the flight tube. To a first approximation this is accomplished by subtracting the mass spectrum offset in μs from the arrival time of the parent ion, and then subtracting an additional 4.5 μs to obtain the time at which the parent ion is in the excitation region, labeled as such in Figure 2-1. Frequently a small photo-induced but non-resonant background is observed in the photodissociation spectrum which can aid in refining the overlap timing somewhat. Once the approximate timing has been calculated, a laser scan can be initiated and a resonant photodissociation event discovered. Once found, the laser can be fixed on the transition and the overlap timing changed to optimize the photodissociation signal.

It is not always possible to find a resonant photodissociation event. When the excited state lifetime is greater than 10 μs, the parent ion will impact the detector before dissociating resulting in a featureless spectrum. The optimal lifetime will be sufficiently long to allow for both vibration and rotation of the molecule, resulting in a photodissociation spectrum exhibiting both vibrational progressions and rotational structure.

Two-Color Experiments

The initial phase of the two-color experiment is to optimize the timing of the pump laser in the same fashion discussed previously. Once this has been accomplished, the relative timing of the dump laser can be determined. Typically, the timing of the dump laser relative to the pump laser is scanned while the pump is fixed at a resonant frequency and the dump at a non-resonant frequency. The photodissociation signal is monitored as a function of the pump/dump timing offset and the final timing corresponds to the maximum photodissociation intensity. A typical pump/dump offset scan will show a gradual increase in photodissociation signal as the dump laser delay increases followed by a rapid drop off when the delay is longer than the excited state lifetime.

Calibration of Mass Spectra

When kinetic energy (KE) is imparted to the cations by the acceleration stack of the mass spectrometer, the velocity (v) at which the ions travel down the flight tube is mass (m) dependent according to the following equation,

$$KE = \frac{1}{2} mv^2 \qquad (2\text{-}1)$$

Lighter ions, having a greater velocity, will arrive at the detector earlier than the heavier ions. Time-of-flight mass spectra are obtained by monitoring ion-current as a function of time. The arrival time of an ion of a given m/z is a constant for any given time-of-flight mass spectrometer provided the kinetic energy of the acceleration pulse and the length of the flight tube are held constant.

Due to slight variances in the voltage present on the acceleration stack, the mass calibration of the TOF mass spectrometer will not be identical from one day to the next. Calibration of the mass spectra may be accomplished using either of two different techniques. Both methods rely on the markers present in the mass spectrum itself. These markers include the peak which corresponds to the mass of the transition metal cation which is typically the most intense and often arrives earliest at the detector. The background of water, which is always present to some extent, can also be used to identify hydrated metal cations. Other such markers include the peaks corresponding to oxides, the metal dimer and, under some conditions, the metal trimer cations. With experience, these markers are very easily identified and the unknown peaks assigned relative to them.

Based on this method of calibration, a computer program written in the C programming language has been developed. The programs code, TOFMS.c, may be found in

Appendix A. TOFMS reads a mass spectrum file generated by the data acquisition program, and displays it on the computer screen. A cursor can then be placed on a marker peak and the mass of that peak changed to the true mass, resulting in a shift in the entire mass spectrum. This one-point calibration is most effective if the marker peak is chosen to be near the unknown peak so as to minimize calibration error. If no marker exists close to the unknown m/z peak, a calibration utilizing a marker in the center of the mass spectrum will result in a mass accuracy at either m/z extreme which is typically smaller than 0.15 m/z. Once calibrated, the cursor may be moved to unknown peaks to obtain their m/z. This method is sufficient for the identification of the majority of transition metal cluster ions studied. Figure 2-2 shows a computer screen snapshot of a typical mass spectrum of vanadium cluster cations formed in a 1%Ar/99%He expansion.

For more accurate calibration across the entire mass spectrum, a multiple-point calibration may be completed using any of a variety of spreadsheet computer programs. The data file must be imported into the spreadsheet as a delimited text file. The initial time of arrival in μs is equal to SAstop/1000, and the increment in arrival time, also in μs, across the mass spectrum is the Period/1000. From these two parameters an ordinate axis for the intensity

data, which comprises the bulk of the file, can be formed. A linear regression can then be completed with an independent variable equal to the square root of the true mass of the marker peaks and a dependent variable equal to the TOA of each marker peak in the mass spectrum. The entire spectrum can then be shifted using the constants obtained through the regression. Although this method is more tedious than using the program TOFMS, a mass spectrum which is congested with unknown peaks is more easily understood. Figure 2-3 shows a mass spectrum of niobium cluster cations expanded in a 0.5%Kr / 99%He expansion gas which was calibrated using a multiple point regression.

Calibration of Photodissociation Spectra

The raw photodissociation spectra files which are generated by the data acquisition program contain at each resolution element the average intensity of the ion current collected during 16 repetitions of the experimental cycle. In order to calibrate this data the beginning and end points of the laser frequency scan and the scan rate must be recorded. From the scan rate, the laser increment/resolution element can be determined from the following equation:

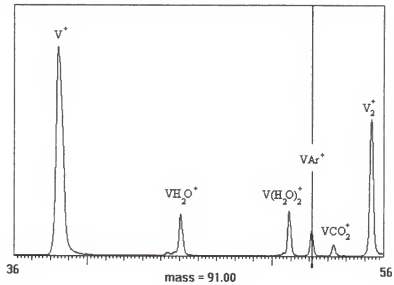

Figure 2-2. Time-of-Flight Mass Spectrum of VAr^+.

The figure shows the screen dump of the TOFMS program with peak assignment included. The horizontal axis displays the arrival time in μs. The line which passes through the VAr^+ peak is the "cursor" which may be used to determine the m/z of unknown peaks once the single point calibration is complete.

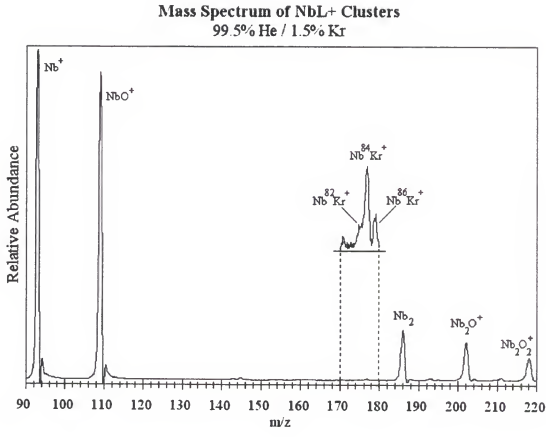

Figure 2-3. Time-of-Flight Mass Spectrum of $NbKr^+$.

The mass spectrum of $NbKr^+$ has been calibrated using the Nb^+, NbO^+, and Nb_2^+ peaks for references. The blow up of the m/z region from 170-180 m/z shows the three isotopomers of $NbKr^+$. The relatively small amount of $NbKr^+$ formed was sufficient to obtain the photodissociation spectra which appear in Chapter 3.

$$Laser\ Increment\ (cm^{-1}) = \frac{16}{9.1}(Scan\ Rate) \qquad (2\text{-}2)$$

where 9.1 is the number of laser shots/second. With the result of equation (2-2) the energy axis of the photodissociation spectrum can be constructed resulting in a calibrated spectrum to within the ~5 cm^{-1} accuracy of the laser scan box.

To more accurately calibrate the photodissociation spectra neon optogalvanic transitions are recorded simultaneously with any unknown spectrum. The neon transitions which occur in the visible region are well known and the experimentally observed and literature values [11,12] are shown in Figure 2-4. The line positions of the experimental obtained neon transitions can be fit to the literature values through a linear regression and the offset determined applied to the energy axis.

The final step in the calibration process is to Doppler correct the spectrum [13] into the rest frame of the detector. The Doppler shifted frequency (υ) may be determined from the following relationship:

$$\upsilon_{Doppler} = \upsilon_{obs}\left(1 + \frac{1.3891\sqrt{\frac{V}{m}}}{c}\right) \qquad (2\text{-}3)$$

where ν_{obs} is the observed frequency in wavenumbers, V is the kinetic energy imparted by the acceleration stack in volts, m is the mass in amu, and c is the speed of light in cm/μs.

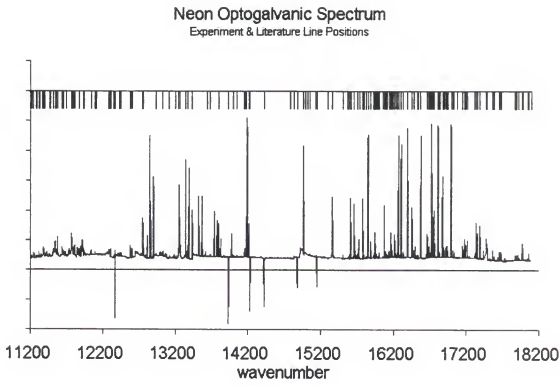

Figure 2-4. Neon Optogalvanic Transitions.

The experimentally observed neon optogalvanic transitions in the 11200-18200 cm^{-1} region typically scanned are shown while the literature values are displayed as tick marks above the spectrum. The intensity of the observed transitions are dependent on the laser power and the voltage applied to the optogalvanic cell. The positive or negative direction of the experimentally observed transitions correspond to a photo-induced increase or decrease in the number of charge carriers present in the discharge.

CHAPTER 3
SIMULATION OF ROTATIONAL SPECTRA

A portion of this dissertation encompasses the interpretation of the rotationally resolved spectra of ligated transition metal diatomic cations. Of the molecules studied in this dissertation VAr^+, $NbAr^+$ (Chapter 4) and CoO^+ (Chapter 6) each exhibit partially resolved rotational structure which has allowed for determination of the ground and excited state bond lengths and the vibration-rotation coupling constants. The partial resolution of the bands observed has made it necessary to develop a method of fitting them which does not rely upon the conventional analysis using combinational differences [1]. This chapter presents the theoretical aspects behind the computer program written to facilitate the rotational analyses completed. Additionally, the "tricks of the trade" which aided in the fitting procedure will be described.

Rotational Energy Levels

For a vibrating diatomic molecule which undergoes an optical transition between the vibrationless level of the

ground state and an excited electronic state, the excitation energy is given by:

$$\nu = \nu_{00} + \omega_e(v'+1/2) - \omega_e x_e(v'+1/2)^2 + B_v J'(J+1) - B_0 J''(J''+1) \qquad (3-1)$$

where ν_{00} is the origin of the electronic transition, ω_e and $\omega_e x_e$ are the vibrational frequency and anharmonicity of the excited state, {B', B''} and {J', J''} are the excited and ground state rotational constants and quantum numbers, and α_e is the vibration-rotation coupling constant. The rotational and vibrational terms are separable from one another so that the rotational structure of a given band with respect to the origin of the vibrational transition is given by:

$$\upsilon(J',J'') = B_v J'(J+1) - B_0 J''(J''+1) \qquad (3-2)$$

Typically, the rotational transitions are categorized by the difference $\Delta J=(J'-J'')$ allowing Equation 3-2 to be re-written as a function of only J'':

$$\upsilon_P = -(B_v+B_0)J'' - (B_v-B_0)J''^2 \qquad (3-3)$$

$$\upsilon_Q = (B'_v-B''_0)J''(J''+1) \qquad (3-4)$$

$$\upsilon_R = 2B_v + (3B_v - B_0)J'' + (B_v - B_0)J''^2 \qquad (3\text{-}5)$$

where the P, Q and R branches correspond to ΔJ=-1, 0, 1. For bands which are resolved to the extent that the individual members of the P, Q and R branches can be identified and fit to Equations 3-3 through 3-5, determination of the ground and excited state rotational constants is straight-forward. However as shown in Figure 3-1, as the difference (B'-B'') increases the branch structure may "turn-around" and overlap, causing the individual transitions to become obscured. In instances where this is the case, a simulated contour of the band may be generated by convoluting an instrument function onto the calculated line-positions. The residual of the calculated band-shape to that of the experimental spectrum can be minimized by varying the rotational constants and a few other relevant parameters which will be introduced in the following sections.

Effect of Total Angular Momentum

In addition to the rotational constants, B' and B'', the ground state total angular momentum (orbit + spin), Ω'', and change upon excitation, ΔΩ, effect the observed

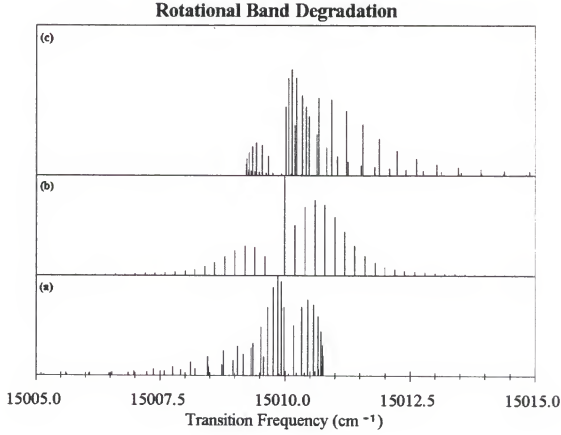

Figure 3-1. Relationship Between Band Degradation and (B'-B'')

Depending on the relative size of the upper and lower state rotational constants either the R- or P-branch transitions will pile-up and turn around resulting in a head. (a) When B'' is less than B', a head will form in the P-branch and the band is blue-degraded. (b) When B''=B', there is no head formed. (c) When B'' is greater than B', a head will form in the R branch and the band is red-degraded.

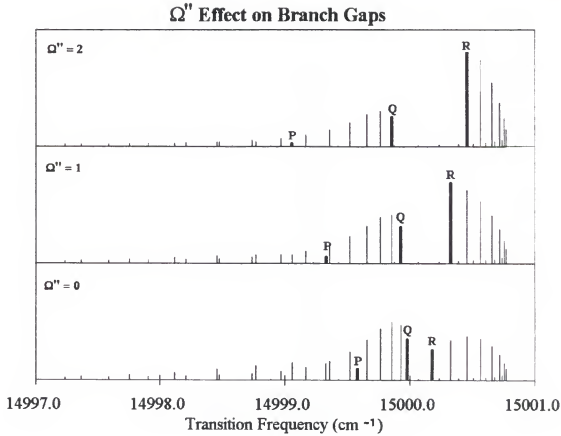

Figure 3-2. Effect Of Ω'' On Branch Structure

As the ground state total angular momentum increases the transitions with J'' less than Ω'' are no longer present, creating gaps between the first members of the P, Q and R branches and the band origin. As Ω'' increases, the size of the gaps increase.

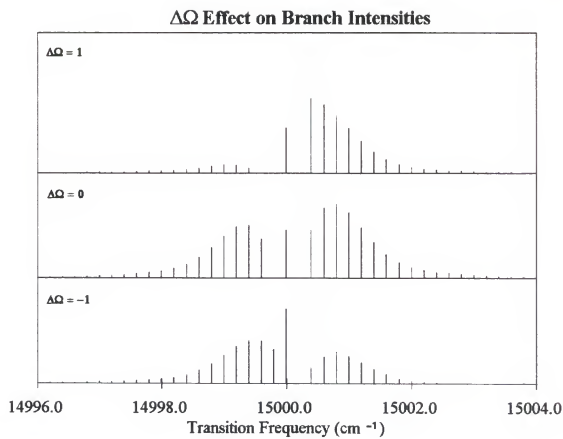

Figure 3-3. Effect of ΔΩ On The Branch Intensities

The change in electronic angular momentum, ΔΩ, which takes on the values of ±1 or 0, determines in conjunction with Ω'' and J'' the line-strengths of the branches relative to each other. If ΔΩ is +1 or -1, the intensities of the R- and P-branches increase respectively. A ΔΩ=0 causes the Q-branch to increase in intensity.

rotational structure. As the ground state total angular momentum increases, Figure 3-2, the transitions with J'' less than Ω'' are no longer present, creating gaps between the first members of the P, Q and R branches and the band origin. This occurs due to the rotational selection rule that J'' must be larger or equal to Ω''. The ΔΩ, which takes on the values of ±1 or 0, determines in conjunction with Ω'' and J'' the line-strengths of the branches relative to each other as predicted by the Hönl-London factors [reference Herzberg]. Although the Hönl-London factors give the line strengths for symmetric top singlet-singlet transitions, their application to the multiplet-multiplet transitions of Chapters 4 and 5 appear to predict the observed intensities accurately. The effect of ΔΩ on the relative intensities of the branches is shown in Figure 3-3.

Effect of Temperature

The intensities of the rotational transitions are dependent not only upon the total angular momentum, but also upon the internal energy of the ground state ions. The cold ions produced by the supersonic expansion source possesses a minimum of vibrational energy, which explains the fact that it is extremely rare to observed hot-bands, transitions from excited vibrational levels of the ground state complexes, in our spectrometer. However, rotational temperatures on the

order of 2-10 Kelvin are common. The populations of the rotational energy levels as a function of J (N_J) following supersonic expansion have been shown to be well described by a combination of two different Boltzmann distributions:

$$N_J = (1-x)e^{\frac{-BJ(J+1)}{kT}} + xe^{\frac{-BJ(J+1)y}{kT}} \qquad (3-6)$$

where x is the "hot" fraction of the ions, y is the ratio of the lower to higher rotational temperature and k is the Boltzmann constant. As the supersonic expansion propagates, the number density of collisional species in the beam decreases. Once the cluster cations enter the collision-free region, no energy can flow from the internal degrees of freedom of the molecules to the carrier gas. Consequently, a portion of the cluster cations formed do not have the opportunity to quench the rotational energy "frozen in" by the expansion. The freezing in of rotational energy into this small fraction of the total ion ensemble, typically 5%, requires the second Boltzmann distribution which utilizes a temperature 3-6 times higher.

Rotational Spectrum Simulator

A computer program based upon the theory and concepts presented in this chapter has been written in Microsoft C,

Version 5.1 for the DOS operating system. The program code appears in Appendix A in addition to a listing of the commands currently supported. A screen dump of the application is shown in Figure 3-4. The parameters Ω and $\Delta\Omega$ are labeled as K and delK respectively in the program heading because the symbols are not supported by the compiler. The user has the choice of displaying any combination which includes the experimental spectrum, calculated line-positions, and the simulated contour produced by the convolution of a gaussian line-shape onto the calculated line-positions. Each of the parameters which effect the rotational line positions appear at the top of the spectrum in units of wavenumbers. Menus are accessible which allow for changing the number of rotational levels calculated and the resolution of the instrument function. Once a spectrum is fitted, the contour and calculated line-positions can be written to a delimited text file.

Fitting Procedure

The first step in determining the rotational constants of the ground and excited states of the complex, is to determine a starting point for each. For the systems studied in chapters 4 and 6, theoretical calculations have been completed and bond lengths have been reported. These

bond lengths can be converted into rotational constants and utilized as a first approximation through the application of:

$$B = \frac{16.8576314}{\mu r^2} \quad cm^{-1} \tag{3-7}$$

where μ is the reduced mass in atomic mass units and r is the bond length in angstroms. Unfortunately, most theoretical investigations report only ground state spectroscopic constants. Although the lack of excited state information can make analysis more difficult, trends in the experimental photodissociation spectrum can be utilized in to predict the difference between the ground and excited state rotational constants. For example, it is apparent from Equations 3-2 through 3-4 that each branch has a term in (B'-B'') which is dependent upon J^2. When sharp rotational transitions are observed, as is case in the rotationally resolved $NiAr^+$ spectrum shown in Figure 3-5, the line positions can be fit as a function of J and J^2, and the difference in upper and lower rotational constants determined from the quadratic dependence. If the rotational spectrum is not sufficiently resolved to obtain the line-positions of a single branch, but a band-head is observed,

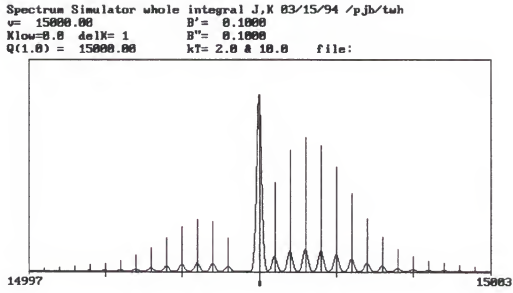
<1K> Spectrum Simulator whole integral J,K 03/15/94 /pjh/twh
v= 15000.00 B'= 0.1000
Klow=0.0 delK= 1 B''= 0.1000
Q(1.0) = 15000.00 kT= 2.0 & 10.0 file:
14997
15003

Figure 3-4. Screen Dump of Rotational Simulator

The rotational simulation program showing calculated line positions and contour. The band origin (v), rotational constants (B'' and B'), temperatures of the two Boltzmann distributions (kT), ground (K)and change in total angular momentum (delK), are all visible at the top of the simulation.

the relative size of the rotational constants can be determined. When the rotational transitions trail-off to the red energy side of the spectrum as in Figure 3-5, the upper-state rotational constant is less than that of the ground-state and the transition is "red-degraded". The converse of this occurs, resulting in a "blue degraded" spectrum, when the upper-state rotational constant is greater than that of the ground state.

After suitable starting points are determined for the rotational constants, they can be refined until the calculated line-positions overlap with the experimental spectrum. This procedure may entail shifting the band origin and changing the total angular momentum of the ground state in addition to changing the rotational constants themselves. If an accurate value of (B'-B'') has been determined, this difference can be preserved and the lower or upper state constant changed until the experimental line positions are fit. In the majority of cases, superimposing the instrument function upon the calculated intensities and choosing an appropriate resolution element will greatly simplify the fitting process. In particular, the use of the instrument function greatly aids in the fitting of the spectrum in the region of the band head, where the overlap of many transition obscures the individual transitions.

Fitting the intensities of the transitions is most

easily refined after the instrument function is superimposed upon the calculated line-positions. The assignment of $\Delta\Omega$ is usually obvious, given that only three possibilities ($\pm 1,0$) exist. A value of $\Delta\Omega$ of +1 causes the R branch to be the most intense, while a value of -1 or 0 causes the P and Q branch intensities respectively to dominate. The temperature of and relative ratio of the two Boltzmann distributions may be determined by an iterative process, however values of 2K and 10K with a hot-fraction of 5% provides a good starting point.

Errors in Rotational Constants and Bond Lengths

The error limits reported in the rotational constants and bond lengths reflect the smallest deviation in rotational constants which results in an incorrectly fit spectrum. In practice assigning the error limits entails ramping up and down the rotational constants to determine when the experimental spectrum is no longer fit. The upper and lower limits of the rotational constants can then be converted to a bond length by application of Equation 3-7 to generate the error associated with the bond length determined. The error limits are not calculated, but are dependent upon the perceptions of the person fitting the spectrum. If a large number of transitions are observed and

fit, the accuracy of the fit is increased and reflected in the reported constants. When the rotational transitions are well resolved, the residual of the calculated to experimental band contour is more easily evaluated, and the error limits reported reflect this.

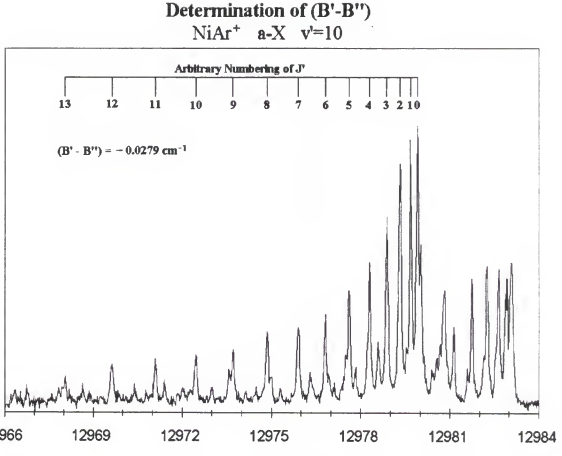

Figure 3-5. Determination of (B'-B'') From Branch Structure

The rotationally resolved spectrum of the v'=10 band in the a-state of $NiAr^+$. The clearly evident branch structure labeled by arbitrary assignment of J'' allows for a regression in J'' and $(J'')^2$ to be completed where the coefficient of $(J'')^2$ is the difference (B'-B'').

CHAPTER 4
PHOTODISSOCIATION OF GROUP VB METAL-RARE GAS CATIONS

In recent years their has been increased interest concerning the properties and reactions of clusters containing transition metal cations. Much of this research has focused on small gas-phase cationic systems which can be interrogated using ion beam and mass spectrometric techniques [14,15,16]. The simplest of such ionic clusters contain but a single transition metal cation and a neutral ligand species held together by at least a charge-(induced dipole) association. A ligated transition metal complex may be used as a simple model of solvation affording an understanding of the inductive forces important in the condensed phase. In addition, insight into the chemistry which takes place on surfaces, including surface adsorption, can be obtained.

Previous work with cluster cations has included collision-induced dissociation (CID) studies [17,18] where the energy required to sequentially remove neutrals from a cluster cation have been determined. The CID technique has also allowed for determination of the ground state binding energies of various ligands to single transition metal

cations [19,20] by monitoring the kinetic energy dependencies that ion-neutral reactions exhibit. Other researchers have utilized equilibrium techniques [21,22] to determine bond enthalpies. In equilibrium studies, bond dissociation energies are extracted from the rate constants of a cation reacting with a neutral species as a function of temperature. The disadvantage of the equilibrium method is that the vibrational frequencies of both the reactants and products are required to convert the reaction enthalpy to a bond energy. If experimental frequencies are not available, an error on the order of 350cm^{-1} [22] or more may be introduced into the binding energy. For the charge-(induced dipole) complexes presented in this chapter, a 350 cm^{-1} inaccuracy would result in a 20% or larger error in binding energy.

Important chemical processes do not only occur when the species involved are in their ground states, but also when the systems are electronically excited, requiring knowledge of the excited state potential energy surfaces. For example, a glow-discharge [23,24] typically generates electronically excited transition metal-rare gas diatomic and cluster ions. Matrix-isolation [25,26] is also a popular technique which can utilize rare gas atoms as a non-reactive medium in which to deposit transition metal containing molecules. Although the noble gases are viewed

as being inert, this is not the case. A transition metal cation can be bound to a noble gas by more than 0.5 eV, and the binding is not constant but dependent upon the electronic state of the metal cation. It seems appropriate, then, to require the potential energy surface of the transition metal-rare gas cations to be understood prior to the analysis of matrix isolated species, particularly when electronic transitions are involved. Although the thermodynamic studies previously mentioned can indicate a chemical process to be dependent on the excited state of the precursor, the unambiguous identification and properties of the excited state can not be determined.

High resolution photodissociation spectroscopy coupled with ion beam techniques is not subject to the limitations imposed by the thermodynamic methods. Both ground and excited state binding energies [4,5,6,7] can be determined and accurate assignment of the excited states made. When rotational resolution is achieved [8,9,10], the bond lengths of the species in both the ground and excited states involved in a transition can be determined. In addition, the vibrational frequencies and rotational constants required to parameterize the excited state potential can be determined.

The following chapter presents the rovibronic analysis of the photodissociation spectra obtained for the Group VB

metal-noble gas cations. This study is unique in that the trends observed in the spectroscopic constants for a common group can be presented as a function of both metal chromophore and ligand. The potential energy surface of the B-state of VAr^+ has been parameterized using three popular analytic potential energy functions, and the ability of each to replicate the experimental data is evaluated.

Vibrational Structure of Electronic Spectra

Figures 4-1 to 4-6 show the resonant photodissociation spectra of VAr^+[27], $NbAr^+$[28], $TaAr^+$, VKr^+[27], VXe^+ [29], and $NbXe^+$[30] as a function of laser frequency. At these energies no noble gas cations are observed as photoproducts, as would be expected from the large disparity in the ionization potentials of the noble gas ligands (IP(Ar)= 15.755 eV, IP(Kr)= 13.996 eV, IP(Xe)= 12.130 eV) relative to the transition metals (IP(V)=6.74 eV, IP(Nb)=6.88 eV, IP(Ta)= 7.89 eV)[31]. In each figure the tick marks above the spectra indicate progressions in excited state vibrational quanta. The state labels (ie. B-X) have been chosen to be consistent throughout the figures, (upper state designation)-X, where the upper-state letter denotes dissociation of the complex into a transition metal cation

in a specific electronically excited state and a ground state noble gas. The X is by convention the label given to the ground state. An upper-case excited state designation implies a spin-allowed transition centralized on the transition metal cation (ie. $\Delta S=0$), and a lower-case a spin-forbidden transition.

Vibrational Analysis of Electronic Spectra

The vibrational progressions evident in Figures 4-1 to 4-6 have been fit to the standard equation [1]

$$E(v') = T_{e0} + \omega_e(v'+\frac{1}{2}) - \omega_e x_e(v'+\frac{1}{2})^2 \qquad (4\text{-}1)$$

from which the band origins, T_{eo}, vibrational frequencies, ω_e, and anharmonicities, $\omega_e x_e$, are derived. The zero of energy for the fits is taken to be the zero-point level of the ground electronic state. No "hot bands" resulting from transitions from excited vibrational levels of the ground states were identified. The accuracy with which Equation 4-1 describes the observed vibrational structure depends on the existence of any perterbations between the excited states and ground state and the degree of anharmonicity present in the excited state potential. To facilitate the

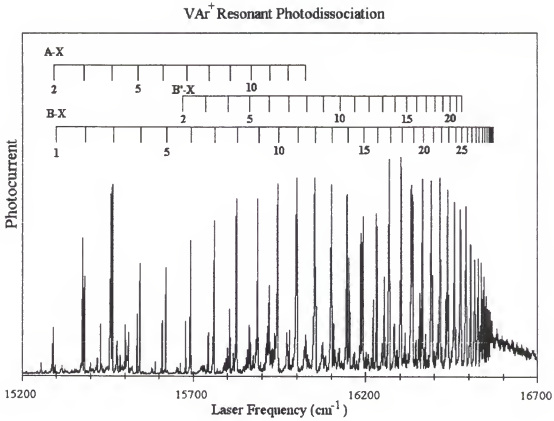

Figure 4-1. Photodissociation Spectrum of VAr^+

The photodissociation spectrum of VAr^+ in the visible region. The horizontal axis of this figure is the dissociation laser frequency and the vertical scale is the relative V^+ photocurrent resulting from the photodissociation of VAr^+. The tick marks above the spectrum indicate the excited states observed and their vibrational numbering.

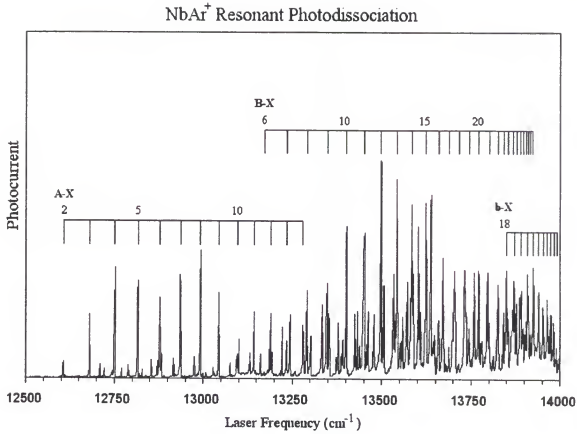

Figure 4-2. Photodissociation Spectrum of $NbAr^+$

The photodissociation spectrum of $NbAr^+$ in the visible region. The horizontal axis of this figure is the dissociation laser frequency and the vertical scale is the relative Nb^+ photocurrent resulting from the photodissociation of $NbAr^+$. The tick marks above the spectrum indicate the excited states observed and their vibrational numbering.

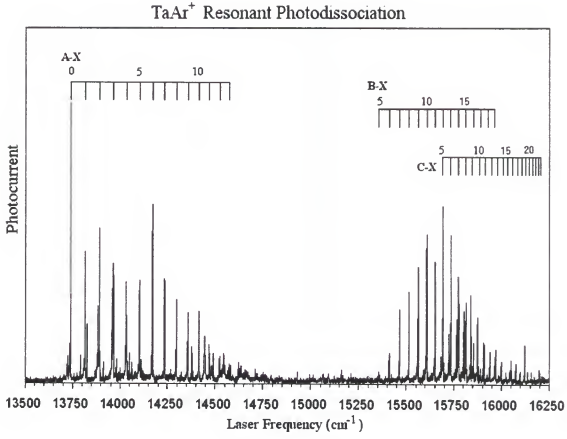

Figure 4-3. Photodissociation Spectrum of $TaAr^+$

The photodissociation spectrum of $TaAr^+$ in the visible region. The horizontal axis of this figure is the dissociation laser frequency and the vertical scale is the relative Ta^+ photocurrent resulting from the photodissociation of $TaAr^+$. The tick marks above the spectrum indicate the excited states observed and their vibrational numbering.

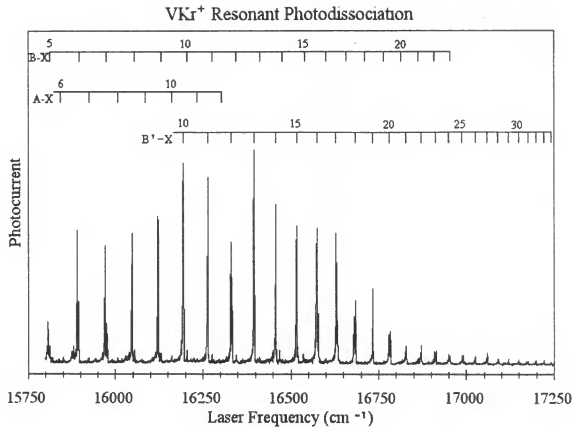

Figure 4-4. Photodissociation Spectrum of VKr^+

The photodissociation spectrum of VKr^+ in the visible region. The horizontal axis of this figure is the dissociation laser frequency and the vertical scale is the relative V^+ photocurrent resulting from the photodissociation of VKr^+. The tick marks above the spectrum indicate the excited states observed and their vibrational numbering.

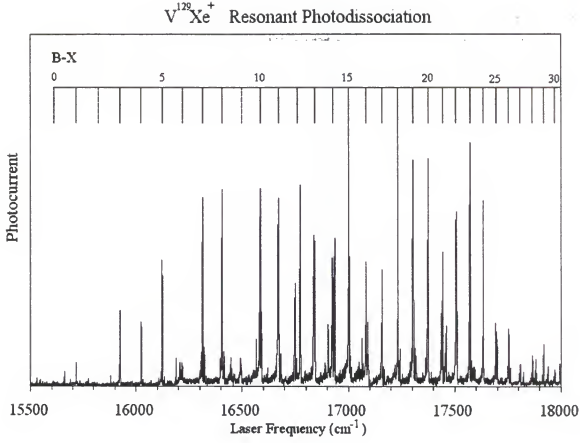

Figure 4-5. Photodissociation Spectrum of VXe^+

The photodissociation spectrum of VXe^+ in the visible region. The horizontal axis of this figure is the dissociation laser frequency and the vertical scale is the relative V^+ photocurrent resulting from the photodissociation of VXe^+. The tick marks above the spectrum indicate the B-X transitions and their vibrational numbering.

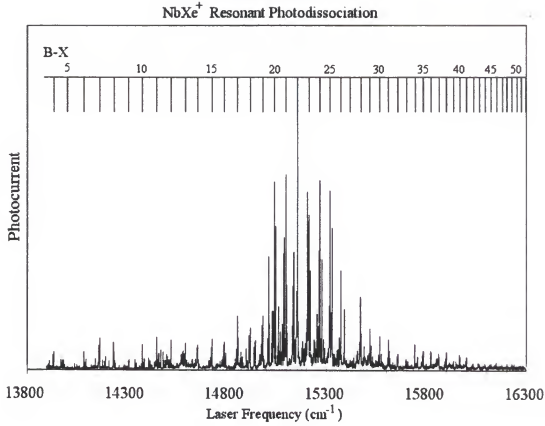

Figure 4-6. Photodissociation Spectrum of $NbXe^+$

The photodissociation spectrum of $NbXe^+$ in the visible region. The horizontal axis of this figure is the dissociation laser frequency and the vertical scale is the relative Nb^+ photocurrent resulting from the photodissociation of $NbXe^+$. The tick marks above the spectrum indicate the B-X transitions and their vibrational numbering.

fitting procedure, perturbations and vibrational levels near the dissociation limit have been omitted to minimize the residuals to the fit near the bottom of the potential. This is of no consequence as a modified treatment for these levels will be presented later.

The experimentally observed transitions and the residuals of the calculated line positions based on the spectroscopic constants of Tables 4-1 through 4-6 and the application of Equation 4-1 are given in Tables 4-7 through 4-12. The fits of the excited states observed to Equation 4-1 are also shown in Figures 4-7 through 4-12. Although the vibrational structure near the bottom of the excited state potentials is accurately reproduced by the tabulated spectroscopic constants and Equation 4-1, the consistent underestimations of the higher vibrational levels for states which converge to a dissociation limit are clearly shown.

The accuracy of the spectroscopic constants is also dependent upon the vibrational numbering, shown above the tick marks in Figures 4-1 through 4-6. The absolute numbering of the vibrational progressions is obtained by fitting the experimentally determined isotopic shifts among the different isotopomers within a common progression to equation 4-2, where ρ is the square root of the ratio of the two isotopomers reduced masses. Theoretical values were used to approximate the vibrational frequencies of the

$$Shift(cm^{-1}) = (1-\rho)\left[\omega_e'(v'+\frac{1}{2})-\omega_e''(v'+\frac{1}{2})\right] \qquad (4\text{-}2)$$
$$-(1-\rho^2)\left[\omega_e x_e'(v'+\frac{1}{2})^2-\omega_e x_e''(v'+\frac{1}{2})^2\right]$$

ground states (w_e'') where available, otherwise a frequency 1.5 to 2.0 times larger than the excited state frequency was chosen. The increased vibrational frequency of the ground state is consistent with the red-degraded nature of the bands observed, which indicates an increased binding energy and vibrational frequency in the ground state. The anharmonicity of the ground state ($w_e x_e''$) was taken to be the same as that determined for the excited state.

Figures 4-13 and 4-14 show the fits of the observed isotopic shifts ($V^{84}Kr^+$-$V^{86}Kr^+$ and $V^{129}Xe^+$-$V^{136}Xe^+$) for the B-state of VKr^+ and VXe^+ to Equation 4-2. The solid curves above and below the line of the best fits serve as brackets which assume the vibrational index to differ by ±1 quantum. The fits shown in Figures 4-13 and 4-14 are representative of those completed on the other excited states observed in the same two complexes and in $NbXe^+$. The vibration numbering is correct to within one vibrational index.

Due to the absence of naturally occurring isotopes of the group VB metals or argon in an abundance large enough to detected in our mass spectrometer, absolute vibrational numbering for VAr^+, $NbAr^+$ and $TaAr^+$ via isotope analysis

could not be determined. Due to the similarities observed between the vibrational structure evident in the spectra of VAr^+ and $NbAr^+$ as compared to VKr^+, a vibrational numbering similar to that determined for VKr^+ was utilized. For $TaAr^+$, the numbering was based upon trends in the intensities of the bands comprising the excited state vibrational structure. If an intense transition marked the first member of an excited state vibrational progression it was labeled as the origin, v'=0, otherwise v'=5 was arbitrarily chosen.

Table 4-1. Spectroscopic Constants of VAr^+

	A	B	B'	X
M^+ Atom	-	$^5P_2$ 13594.73	$^5P_2$ 13594.73	$^5D_0$ 0.0
M^+ Configuration	$3d^3\ 4s^1$	$3d^3\ 4s^1$	$3d^3\ 4s^1$	$3d^4$
Symmetry	-	$^5\Pi_1$	-	$^5\Sigma^+$
T_{00} (cm^{-1})	15115	15216	15206	0
ω_e (cm^{-1})	95.4	90.4	87.1	-
$\omega_e x_e$ (cm^{-1})	1.83	1.56	1.43	-
D_0 (cm^{-1})	1195 ±125	1361 ±15	1283 ±130	2982 ±15
D_0^+ (cm^{-1})	-	16577 ±15	-	2982 ±15
v_D	-	48.8	-	-
B_0 (cm^{-1})	-	0.0889 ±0.0007	-	0.1078 ±0.0007
α_e (cm^{-1})	-	0.00206 ± 0.00005	-	-
r_o (Å)	-	2.91 ±0.02	-	2.64 ±0.02

Table 4-2. Spectroscopic Constants of $NbAr^+$

	A	B	a	b	X
M^+ Atom	-	$^5P_2$	-	$^3G_5$	$^5D_0$
M^+ configuration	-	$4d^3\ 5s^1$	-	$4d^4$	$4d^4$
Symmetry	-	-	-	-	$^5\Sigma^+$
T_{00} (cm^{-1})	12456	12739	11747	-	
ω_e (cm^{-1})	81.2	82.3	84.6	-	-
$\omega_e x_e$ (cm^{-1})	1.55	1.46	0.81	-	-
D_0 (cm^{-1})	1023 ±100	1243 ±15	2170 ±200	-	3106 ±15
D_0^+ (cm^{-1})	-	13941 ±15	-	14026 ±15	3106 ±15
r_o (Å)	-	-	3.02 ± 0.02 (v′=4)	-	2.67 ± 0.02

Table 4-3. Spectroscopic Constants of $TaAr^+$

	A	B	C	D	X
M^+ Atomic Limit	$^5D_1$ 13475.40	$^5D_2$ 14494.90	$^3D_1$ 14627.75	-	$^5F_0$ 0.0
M^+ Configuration	$5d^4$	$5d^4$	$5d^3\ 6s^1$	-	$5d^3\ 6s^1$
T_{00} (cm^{-1})	13662	14958	15401	15672	-
ω_e (cm^{-1})	79.3	73.1	66.6	42.2	-
$\omega_e x_e$ (cm^{-1})	1.08	1.39	0.79	0.48	-
D_0 (cm^{-1})	1581 ±15	1116 ±15	888 ±15	908 ±90	1794 ±15
D_0^+ (cm^{-1})	15242 ±50	16075 ±50	16289 ±15	-	1661 ±15

Table 4-4. Spectroscopic Constants of VKr^+

	A	B	B′	X
M^+ Atomic Limit	-	$^5P_2$ 13594.73	$^5P_2$ 13594.73	$^5D_0$ 0.0
M^+ Configuration	-	$3d^3\ 4s^1$	$3d^3\ 4s^1$	$3d^4$
T_{00} (cm^{-1})	15287	15363	15391	-
ω_e (cm^{-1})	101.8	96.6	92.6	-
$\omega_e x_e$ (cm^{-1})	1.31	1.22	1.01	-
D_0 (cm^{-1})	1934	2050 ±15	2022	3818 ±15
D_0^+ (cm^{-1})	-	17413 ±15	17413 ±15	3818 ±15

Table 4-5. Spectroscopic Constants of VXe^+

	B	X
M^+ Atomic Limit	$^5P_2$ 13594.73	$^5D_0$ 0.0
M^+ configuration	$3d^3\ 4s^1$	$3d^4$
T_{00} (cm^{-1})	15613	-
ω_e (cm^{-1})	107.9	-
$\omega_e x_e$ (cm^{-1})	0.95	-
D_0 (cm^{-1})	3220 ±15	5240 ±15
D_0^+ (cm^{-1})	18835 ±15	5240 ±15

Table 4-6. Spectroscopic Constants of $NbXe^+$

	B	X
M^+ Atomic Limit	$^5P_2$ 13594.73	$^5D_0$ 0.0
M^+ Configuration	$3d^3\ 4s^1$	$3d^4$
T_{00} (cm^{-1})	13601	-
ω_e (cm^{-1})	85.2	-
$\omega_e x_e$ (cm^{-1})	0.63	-
D_0 (cm^{-1})	3051 ±15	5815 ±15
D_0^+ (cm^{-1})	16651 ±15	5815 ±15

Table 4-7. Line Positions of the VAr^+ Excited States

v′	A-X	obs-calc	B-X	obs-calc	B′-X	obs-calc
2	15293.7	-1.82	15384.9	-0.20		
3	15380.1	0.19	15467.2	-0.89		
4	15462.1	1.33	15547.3	-0.04		
5	15539.3	1.42	15623.1	0.15		
6	15612.3	0.97	15695.3	0.31	15667.9	-1.51
7	15681.1	-0.02	15763.9	0.36	15735.4	-1.13
8	15746.5	-0.75	15829.1	0.44	15801.9	1.10
9	15808.9	-0.88	15890.9	0.48	15864.9	2.71
10	15867.7	-0.85	15948.5	-0.41	15920.9	0.08
11	15922.7	-1.07	16004.0	-0.25	15976.9	0.42
12	15975.3	-0.01	16055.7	-0.69	16029.8	0.48
13	16024.6	1.47	16104.2	-1.23	16078.4	-0.92
14			16149.3	-2.21	16127.4	0.97
15			16195.9	1.32	16169.0	-1.71
16			16235.7	0.81	16210.6	-1.47
17			16272.8	0.42	16250.9	0.30
18			16306.9	-0.26	16286.1	-0.23
19			16341.0	1.73	16319.0	-0.17
20			16368.9	0.12	16349.2	0.11
21			16398.5	2.66	16377.2	0.96
22			16420.1	-0.35	16402.7	2.21
23			16442.3	-0.42	16425.4	3.58
24			16461.8	-0.84	16445.9	5.48
25			16479.2	-1.14	16464.6	8.52
26			16495.2	-0.76	16480.5	11.62
27			16508.6	-0.88		
28			16520.3	-0.60		
29			16530.7	0.25		
30			16539.7	1.49		
31			16547.1	3.05		
32			16553.4	5.08		
33			16558.6	7.81		
34			16562.8	11.04		
35			16566.3	15.14		
36			16569.0	19.82		
37			16571.2	25.45		

Table 4-8. Line Positions of the NbAr* Excited States

v'	A-X	obs-calc	a-X	obs-calc	b-X	obs-calc	B-X	obs-calc
2	12606.9	-1.86	11911.2	-0.25				
3	12680.5	-0.14	11991.2	0.00				
4	12751.7	2.31	12070.9	1.52				
5	12816.6	1.49	12144.4	-1.45				
6	12878.4	0.76	12220.6	-0.14			13172.4	0.78
7	12936.4	-0.73	12293.3	-0.65			13234.2	0.75
8	12992.5	-0.88	12367.3	1.74			13291.3	-1.08
9	13044.5	-2.17	12434.9	-0.76			13346.8	-1.59
10	13097.2	0.47					13401.6	0.18
11	13142.9	-0.85					13451.6	0.08
12	13189.3	1.61					13498.4	-0.28
13	13234.3	5.86					13543.2	0.20
14	13280.0	13.90					13584.9	0.58
15							13625.9	1.33
16							13659.0	0.76
17							13704.8	-1.72
18					13849.2	-	13732.4	-4.30
19					13871.5	-	13758.9	-2.61
20					13891.0	-	13780.1	0.87
21					13909.3	-	13801.1	9.58
22					13925.4	-	13825.7	16.13
23					13939.8	-	13841.0	16.46
24					13952.6	-	13853.9	17.37
25					13963.9	-	13867.6	21.95
26					13973.8	-	13878.1	26.24
27					13982.4	-	13889.0	33.89
28					13990.3	-	13896.9	41.53
29							13904.8	52.02
30							13911.4	64.16
31							13917.2	78.46
32							13921.7	94.35

Table 4-9. Line Positions of the $TaAr^+$ Excited States

v'	A-X	obs-calc	B-X	obs-calc	C-X	obs-calc	D-X	obs-calc
0	13741.0	0.52					17471.4	0.01
1	13816.9	-0.70					17606.9	0.34
2	13892.9	0.31					17728.8	-1.07
3	13965.6	0.10					17842.3	1.08
4	14037.2	1.03					17940.3	-0.37
5	14103.1	-1.67	15354.5	-0.26	15681.7	-0.16		
6	14170.7	-0.40	15411.3	0.10	15723.5	0.07		
7	14235.3	-0.10	15465.2	0.31	15763.6	0.15		
8	14297.9	0.44	15516.1	0.24	15801.7	-0.13		
9	14357.9	0.49	15564.0	-0.03	15838.8	0.25		
10	14415.8	0.60	15608.9	-0.46	15873.8	0.12		
11	14470.7	-0.06	15651.9	-0.10	15907.0	-0.24		
12	14524.1	-0.14	15691.9	0.09	15939.1	-0.09		
13	14575.3	-0.34	15729.0	0.12	15969.3	-0.17		
14					15998.3	0.14		
15					16025.5	0.18		
16					16050.6	-0.18		
17					16074.6	-0.05		
18					16097.0	0.09		
19					16118.6	1.06		
20					16138.1	1.55		
21					16155.7	1.76		
22					16172.2	2.49		
23					16187.0	0.45		
24					16199.0	-0.12		

Table 4-10. Line Positions of the VKr* Excited States

v'	A-X	Obs-Calc	B-X	Obs-Calc	B'-X	Obs-Calc
5			15807.5	-1.63		
6	15843.8	0.81	15890.9	-0.16		
7	15925.4	-1.17	15971.1	0.49		
8	16006.8	-0.68	16048.6	0.90		
9	16086.9	1.12	16123.5	1.22		
10	16161.8	0.32	16195.1	0.62	16204.9	-0.82
11	16234.3	-0.28	16264.9	0.31	16276.6	0.53
12	16304.9	-0.13	16331.4	0.56	16346	1.71
13			16396.5	-0.40	16412.7	2.06
14			16458.4	-0.69	16469.6	-5.27
15			16518.1	-0.43	16535.9	-1.16
16			16575.0	-1.40	16599.3	2.00
17			16630.1	-1.38	16657.2	1.73
18			16685.2	0.91	16712.0	0.40
19			16734.1	-0.47	16764.6	-1.18
20			16781.1	1.55		
21			16829.0	1.40		
22			16871.7	1.19		
23			16912.9	3.83		
24			16951.1	5.72		
25			16987.8	5.51		
26			17025.6	7.78		
27			17059.8	11.0		
28			17091.1	14.8		
29			17120.8	17.9		
30			17149.0	22.7		
31			17175.7	28.4		
32			17198.4	32.6		
33			17221.1	39.1		

Table 4-11. Band Positions in the VXe^+ B-X System

v'	Observed	Residual
0	-	-
1	15718.9	0.3
2	-	-
3	15925.3	0.4
4	16025.6	0.4
5	16123.9	0.2
6	-	-
7	16314.8	-0.1
8	16407.4	-0.3
9	-	-
10	16586.0	-1.5
11	16671.9	-2.7
12	[16761.4][a]	1.6
13	16841.8	-1.3
14	16925.5	1.1
15	17002.7	-1.3
16	17083.0	1.4
17	17157.3	-0.1
18	17233.1	2.0
19	17304.5	1.4
20	17373.9	0.8
21	17441.6	0.3
22	17506.8	-0.8
23	17571.1	-0.8
24	17634.2	-0.3
25	[17695.9][b]	0.8
26	17753.8	0.1
27	17808.3	-2.2
28	17865.7	0.2
29	17917.4	-1.2
30	17971.3	??

[a] weighted average of two bands at 16748.7 and 16774.0 cm^{-1}

[b] weighted average of two bands at 17692.5 and 17699.2 cm^{-1}

Table 4-12. Band Positions in the NbXe* B-X System

v'	B-X	Residual	v'	B-X	Residual
3	13842.46	-6.29	28	15471.41	-0.80
4	13933.12	4.19	29	15517.90	-2.75
5	14004.65	-3.19	30	15567.92	0.12
6	14088.23	2.75	31	15610.75	-2.94
7	14164.32	2.47	32	15658.11	-0.20
8	14236.35	-0.60	33	15700.82	-0.84
9	14310.53	-0.25	34	15743.59	-0.14
10	14379.61	-3.72	35	15783.89	-0.66
11	14452.04	-2.58	36	15823.73	-0.35
12	14524.75	0.11	37	15861.18	-1.18
13	14595.52	2.13	38	15899.97	0.62
14	14657.55	-3.32	39	15935.98	0.90
15	14728.08	1.01	40	15968.39	-1.15
16	14792.09	0.08	41	16002.01	-0.72
17	14856.88	1.20	42	16035.33	0.68
18	14920.25	2.17	43	16065.49	0.20
19	14982.39	3.19	44	16096.00	1.32
20	15040.39	1.32	45	16123.65	0.87
21	15099.03	1.37	46	16150.17	0.55
22	15156.80	1.82	47	16178.71	3.52
23	15212.07	1.05	48	16204.24	4.75
24	15266.99	1.19	49	16228.30	5.78
25	15318.40	-0.91	50	16252.25	7.97
26	15372.99	1.44	51	16274.61	9.84
27	15420.24	-2.28	52	16295.30	11.32

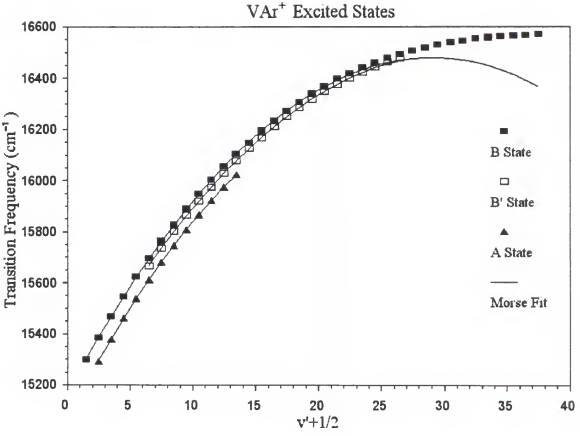

Figure 4-7. Morse Fits of the Excited States of VAr^+

The least-squares fits to Equation 4-1 of the vibrational band origins observed in the VAr^+ spectrum shown in Figure 4-1. The molecular constants obtained from this fit are listed in Table 4-1.

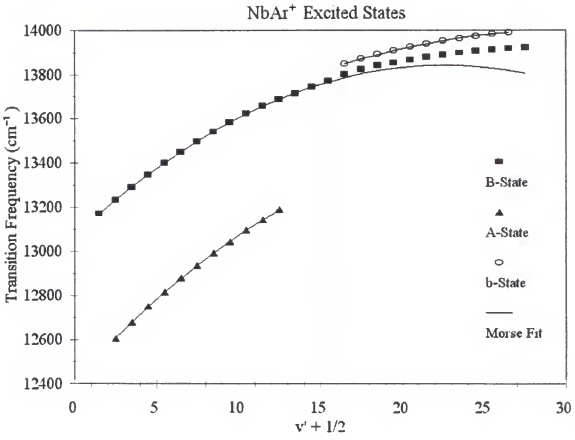

Figure 4-8. Morse Fits of the Excited States of $NbAr^+$

The least-squares fits to Equation 4-1 of the vibrational band origins observed in the $NbAr^+$ spectrum shown in Figure 4-2. The molecular constants obtained from this fit are listed in Table 4-2.

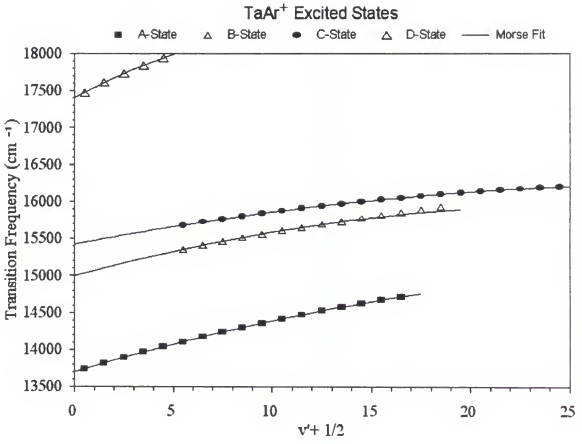

Figure 4-9. Morse Fits of the Excited States of $TaAr^+$

The least-squares fits to Equation 4-1 of the vibrational band origins observed in the $TaAr^+$ spectrum shown in Figure 4-3. The molecular constants obtained from this fit are listed in Table 4-3.

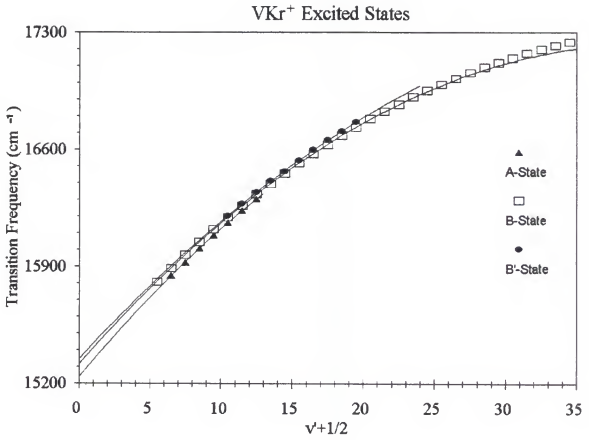

Figure 4-10. Morse Fits of the Excited States of VKr^+

The least-squares fits to Equation 4-1 of the vibrational band origins observed in the VKr^+ spectrum shown in Figure 4-4. The molecular constants obtained from this fit are listed in Table 4-4.

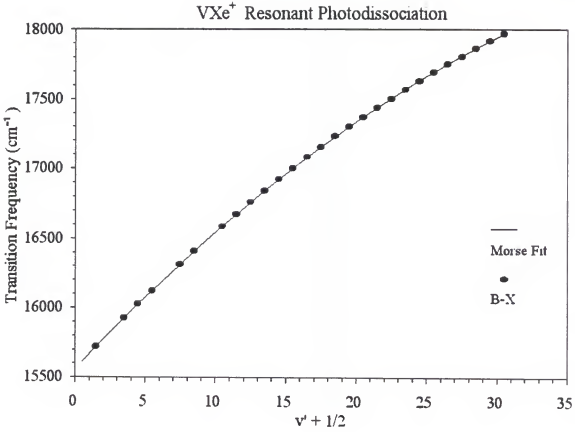

Figure 4-11. Morse Fits of the Excited States of VXe^+

The least-squares fit to Equation 4-1 of the vibrational bands observed for the VXe^+ spectrum shown in Figure 4-5. The molecular constants obtained from this fit are listed in Table 4-5.

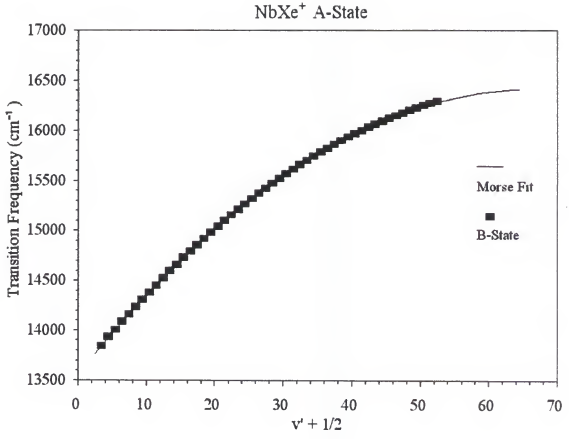

Figure 4-12. Morse Fit of the B-State of $NbXe^+$

The least-squares fit to Equation 4-1 of the vibrational bands observed in the $NbXe^+$ spectrum shown in Figure 4-6. The molecular constants obtained from this fit are listed in Table 4-6.

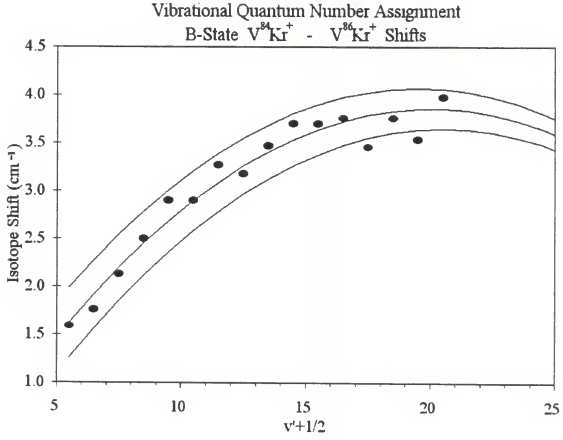

Figure 4-13. Assignment of VKr^{+} Vibrational Numbering Through Isotopic Shifts

The observed $V^{84}Kr^{+}$ - $V^{86}Kr^{+}$ isotope shifts (symbols) plotted as a function of upper-state vibrational quantum number. The calculated solid curve which passes through the center of the data points gives the quantum number assignment of Table 4-10 whereas the remaining two curves serve as brackets and correspond to a vibrational index different by ± 1 quantum.

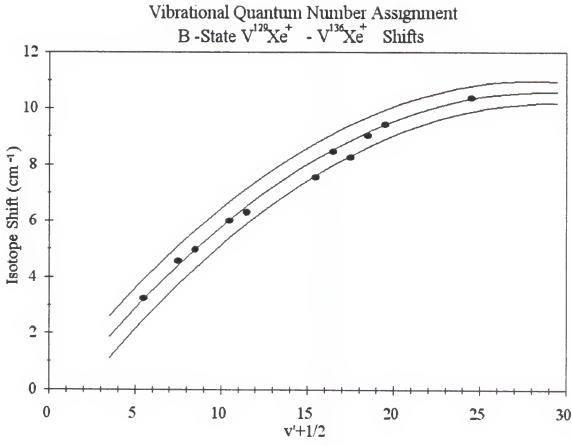

Figure 4-14. Assignment of $NbXe^+$ Vibrational Numbering Through Isotopic Shifts

The observed $Nb^{129}Xe^+ - Nb^{136}Xe^+$ isotope shifts (symbols) plotted as a function of upper-state vibrational quantum number. The calculated solid curve which passes through the center of the data points gives the quantum number assignment of Table 4-11 whereas the remaining two curves serve as brackets and correspond to a vibrational index different by ± 1 quantum.

Determination of Dissociation Energies

As mentioned previously, vibrational levels which approach the dissociation limit are poorly described by Equation 4-1 where the long range charge-(induced dipole) attractive force dominates. Leroy and Bernstein (LB)[32] have developed a method to describe these vibrational levels using a potential energy function of the form:

$$U(r) = repulsiveterms - \frac{C}{r^4} \qquad (4\text{-}2)$$

The C/r^4 term reflects the charge-(induced dipole) nature of the long range attraction where C is fixed as

$$C = \frac{q^2 \alpha}{2} \qquad (4\text{-}3)$$

where q is the charge on the metal cation and α is the polarizability of the neutral ligand (α(Ar)= 1.49 Å^3 [33], α(Kr)= 2.52 Å^3 [34], α(Xe)= 4.11 Å^3 [34]). The vibrational energy levels near the dissociation limit are given by

$$[D - E(v)]^{1/4} = \frac{1}{4} (v_D - v) K \qquad (4\text{-}3)$$

where D is the dissociation energy, E(v) is the energy of

the v^{th} vibrational level, and v_D is the fictitious vibrational quantum number at the dissociation limit. The constant K is a collection of constants including the constant C, the reduced mass of the molecule and a gamma function. It has been shown that the derivative of Equation 4-3 with respect to vibrational quantum number can be approximated by

$$\Delta G(v) = \frac{E(v+1)-E(v-1)}{2} \qquad (4-4)$$

which is related to vibrational binding energy by

$$(\Delta G)^{4/3} = [D - E(v)]\ K^{4/3} \qquad (4-5)$$

Figures 4-15 through 4-17 show the dependence of the derivative of the vibrational energy with respect to the transition frequency for the states observed in the group VB metal-rare gas cations which lead to a convergence. The plot shows $\Delta G^{4/3}$ to be linearly dependent on transition frequency in the vicinity of the dissociation limit, and a linear least-squares extrapolation has been used to obtain the energy of the dissociation limit. The dissociation limits are listed in Table 4-1 through Table 4-6 as D^*.

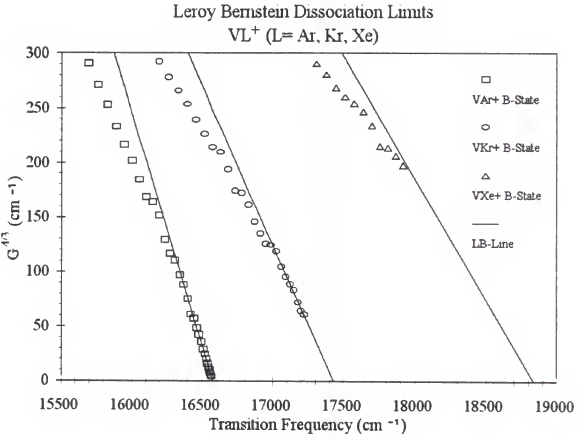

Figure 4-15. Leroy-Bernstein Extrapolations of V^+-Rare Gas Cations

The Leroy-Bernstein extrapolation of the dissociation limits observed for the V^+-rare gas cations. The symbols represent observed values and the solid lines are calculated from a linear least-squares exptapolation of Equation 4-5. The intercept of the calculated lines with the transition frequency axis yield the value of the dissociation limit, D^+, given in Table 4-1 through 4-6.

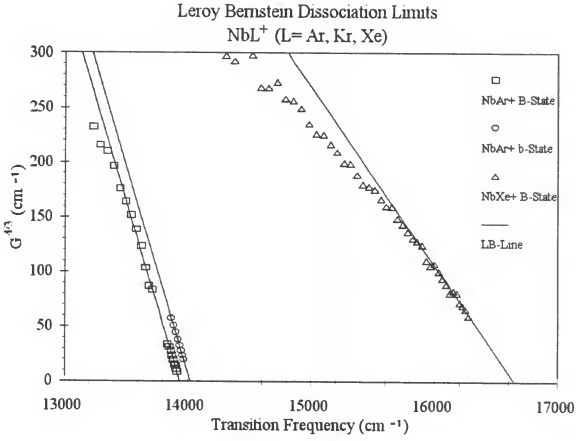

Figure 4-16. Leroy-Bernstein Extrapolations of Nb^+-Rare Gas Cations

The Leroy-Bernstein extrapolation of the dissociation limits observed for the Nb^+-rare gas cations. The symbols represent observed values and the solid lines are calculated from a linear least-squares exptapolation of Equation 4-5. The intercept of the calculated lines with the transition frequency axis yield the value of the dissociation limit, D^*, given in Table 4-1 through 4-6.

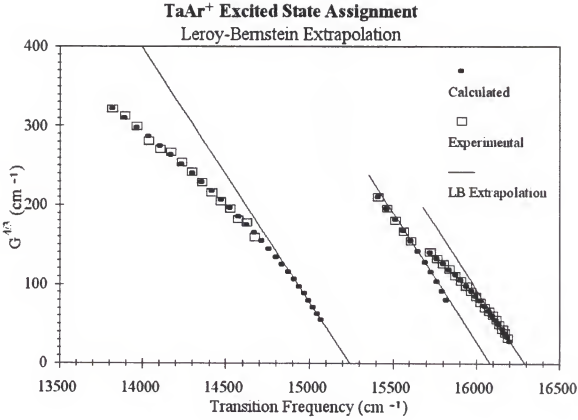

Figure 4-17. Leroy-Bernstein Extrapolations of $TaAr^+$

The Leroy-Bernstein extrapolation of the dissociation limits observed for the Ta^+-rare gas cations. The symbols represent observed values and the solid lines are calculated from a linear least-squares exptapolation of Equation 4-5. The intercept of the calculated lines with the transition frequency axis yield the value of the dissociation limit, D^*, given in Table 4-1 through 4-6.

The dissociation energies (D) of the excited states listed in Tables 4-1 through 4-6 correspond to the difference in energy between the vibrationless level of the excited state and D^*. By comparison of the differences between D^* values and the atomic energy levels of the metal cations [31], the assignment of the atomic components into which the excited states dissociate can be made. The B-state dissociation limits of VAr^+ and VKr^+ have been assigned to $^5P_2$ V^+ and $^1S_0$ (ground state) noble gases. This assignment has been made on the basis of the transition intensities, which appear to be spin-allowed, and the absence of other quintet atomic states within the excitation region. Further evidence for the assignment of the dissociation limit may be inferred from the identity of the B and b-state limits of $NbAr^+$. The assignment of the B and b dissociaiton limits of $NbAr^+$ are quite convincing, the difference in energy between the two limits, 85 cm^{-1}, slightly greater than the 82 cm^{-1} gap between the $^5P_2$ and $^3G_5$ states of Nb^+. The vibrational structrure observed for the B-state of $NbAr^+$, including transition intensities, vibrational frequency and anharmonicity, is similar to those of VAr^+ and VKr^+ supporting their $^5P_2$ V^+ assignment. In addition, the red shift of the electronic origin of the B-state of $NbAr^+$ relative to the origins of the VAr^+ and VKr^+ B-states, approximately 2600 cm^{-1}, correlates quite well

with the 2759 cm^{-1} difference in energy between the V^+ and Nb^+ $^5P_2$ levels. Simular arguments can be applied to the VXe^+ and $NbXe^+$ B-state dissociation limits, which have also been assigned to $^5P_2$ V^+ and Nb^+.

The dissociation limits of the A, B and C-states of $TaAr^+$, shown in Figure 4-17 and given in Table 4-6, have been assigned to $^5D_1$, $^5D_2$ and $^3D_1$ Ta^+ and $^1S_0$ Ar. The A and B state dissociation limits could not be extrapolated directly from experimental data due to a lack of transition being observed near the limits themselves. To fill the void, Equation 4-1 and the constants of Table 4-3 were used to calculated $\Delta G^{4/3}$ near the near the dissociation limit. This approximation relies upon the morse fit to the lower vibrational levels of the excited state potential which is known to under-estimate binding energy and therefore the limits themselves. The difference in energy between the dissociation limits of the A and B-states, 907 cm^{-1}, and the B and C-states, 139 cm^{-1},are expected to be larger than those of the atomic limits and therefore compare favorably with the differences in the $^5D_1$ and $^5D_2$, 875 cm^{-1}, and the $^5D_2$ and $^3D_1$, 133 cm^{-1}, Ta^+ atomic energies.

The remaining excited states for which spectroscopic constants have been reported in Tables 4-1 through 4-6 have not been observed to lead to a band convergence, and the reported excited state dissociation energies have been

determined through a Birge-Sponer approximation, $D_e \approx \omega_e^2/4\omega_e x_e$. The excited state dissociation energies determined using the Birge-Sponer approximation have been corrected so that the zero of energy is the vibrationless level of the excited state.

Once the identity of the excited state dissociation limits have been made, the dissociation energy of the ground states may be determined by subtracting the metal cation promotion energy from the energy of the corresponding dissociation limit (D^*-T_{00}). The ground state dissociation energies are listed in Tables 4-1 through Table 4-6.

It seeem unlikely that the atomic components into which the excited complexes dissociate have been misassigned, especially those derived from the differences between two or more limits. In the case of VAr^+, VKr^+, VXe^+ and $NbXe^+$ however, only single limits has been observed, and therefore it is possible that the B-states do not dissociate into $^5P_2$ V^+, but rather $^5P_3$ or $^5P_1$ V^+ or Nb^+. If this were to be the case, a maximum error of 147 cm^{-1} would result for the vanadiuum complexes and 496 cm^{-1} for $NbXe^+$, which is the difference in energy between the $^5P_3$ and $^5P_2$ V^+ and Nb^+ atomic energy levels. The ± 15 cm^{-1} errors quoted for the excited state dissociation energies in Tables 4-1 through 4-6 assume that the atomic limits have been assigned correctly. For the dissociation energies determined through a Birge-Sponer

approximation, an error of ±10% has been assigned. The ±10% error is consistent with twice the difference between the dissociation energy predicted by a Birge-Sponer approximation and the true LB dissociation enrgy for the B-state of VKr^+.

Rotational Analysis of VAr^+ and $NbAr^+$

Rotational contours of the bands of VAr^+ arise from transitions between rotational energy levels in the ground and excited electronic states. The transition energies can be derived from the energy levels of a symmetric-top rigid-rotor and the overall change in vibrational and electronic energy as [1]

$$\nu(J'', \Delta J) = \nu_0 + B_v'(J''+\Delta J)(J''+\Delta J+1) - B_0''J''(J''+1) \qquad (4\text{-}6)$$
$$\Delta J = +1, 0, -1 \quad \text{[R, Q, P branches]}$$

where ν_0 is the band origin, B_v' and B_0'' are the excited and ground state rotational constants and J" and ΔJ are the ground state rotational quantum number and the change in rotational quantum number upon excitation, respectively. Due to the incomplete resolution of the individual branches, particularly in the region of the band head, an explicit

list of the transition energy of all possible rotational transitions could not be generated from the experimental data. Instead, a rotational contour generated by a computer program written in Standard C (listed in Appendix A), has allowed for the fitting of each band through manipulation of the ground and excited state rotational constants as well as the total angular momentum of the ground state about the bonding axis, Ω'', and the change in total angular momentum upon excitation, $\Delta\Omega$. The relative intensities of the transitions within each band are those given by the Hönl-London factors and the populations of the rotational levels described by a near thermal ensemble. The internal energy distribution actually used is a composite of two different Boltzmann distributions with different characteristic temperatures, which is typical of ions studied in our apparatus [6,9,10]. The distribution used here is 95% a 1.8K Boltzmann distribution plus 5% of an 8K Boltzmann. The two distributions represent the high J 'tail' resulting from the "freezing in" of rotational energy as the collisional energy drops in the last stages of the supersonic expansion.Convolution of a Gaussian instrument function onto the calculated line-positions results in the contour which is compared directly to the experimental bandshape. Furthur details of the simulation may be found in Chapter 3.

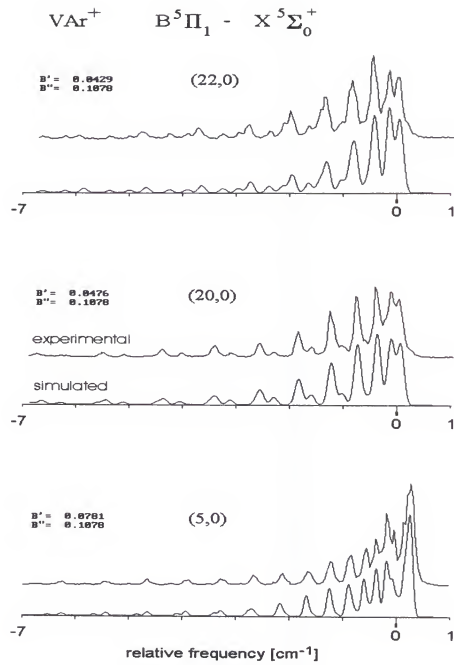

Figure 4-18. Rotational Structure in the B-X System of VAr^+

Rotational structure of several vibronic bands in the **B-X** system of VAr^+. For each band both the experimental photodissociation action spectrum and the simulated absorption profile are shown. All bands have been fit using the same ground state rotational constant.

Figure 4-18 shows the (v',v") = (5,0), (20,0) and (22,0) bands of the B-X system of isolated VAr^+. Both the experimental photodissociation spectrum and simulated rotational contour of each cold band are shown in the figure. The red-degraded bands here are typical of many bands in the visible electronic transitions of vanadium and niobium cation electrostatic complexes and are indicative of a significant lengthening of the bond upon excitation. This electronic transition is perpendicular, involving a change in the electronic angular momentum Ω (Hunds case (c)) from Ω"= 0 in the ground state to Ω'= 1 in the excited state. The analysis of all the bands observed gives a consistent rotational constant of $B_0"= 0.1078\ cm^{-1}$ for the lower level of the transition (v"=0 of the X state), which corresponds to a bond length of 2.64 Å. The excited state rotational constants decrease with increasing v' which can be seen in the decrease of $B_5'= 0.0781\ cm^{-1}$ to $B_{22}'= 0.0429\ cm^{-1}$.

Figure 4-19 shows the vibrational dependence of the upper state rotational constant. To the accuracy of the data, the rotational constants of the B state vary linearly with v'. From this, the vibration-rotation constant, α_e, the negative of the slope of the line in Figure 4-19, is determined to be $(2.06 \pm 0.05) \times 10^{-3}\ cm^{-1}$. Extrapolating the fit line to the fictitious quantum number v'= -1/2

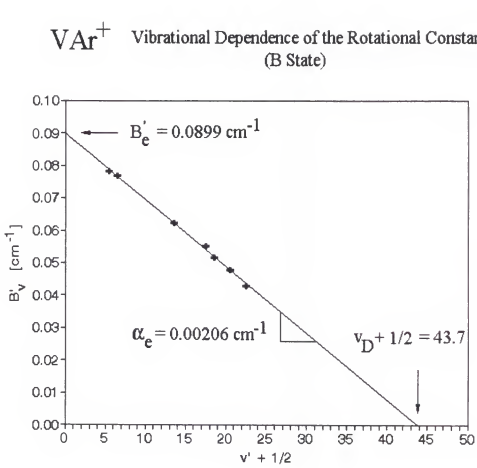

Figure 4-19. Vibrational Dependence of B-X VAr⁺ Rotaional Constants

Vibrational state dependence of the rotational constant of the B state of VAr^+. Observed rotational constants of the upper state int the B-X transition are plotted versus the upper state vibrational numbering ($v' + 1/2$). The linear fit has been extrapolated to the ordinate axis to yield the equilibrium rotational constant bond length of the B state, $B_e = 0.0899\ cm^{-1}$, and thus the equilibrium bond length, $r_e = 2.89 \pm 0.02$ Å. The zero point bond length of the molecule in this state, $r_0 = 2.91 \pm 0.02$, is slightly longer due to the anharmonicity of the potential. The slope of the line in this figure is the vibration-rotation coupling constant, $\alpha_e = (2.06 \pm 0.05) \times 10^{-3}$. The x intercept of the fit line gives the predicted value of the largest possible bound vibrational level, $v_D = 43.2$, where the bond length becomes infinite.

(v'+1/2=0) provides the rotational constant at the equilibrium configuration of the excited state of $B_e' = 0.0899\ cm^{-1}$ which corresponds to an equilibrium bond length of 2.89±0.02 Å. The vibrationless or zero-point level of the same excited state, r_0, is slightly longer due to the anharmonicity of the potential surface, and is found to be 2.91±0.02 Å. Table 4-13 lists the band positions and rotational constants for bands in the B-X system and Table 4-1 lists the spectroscopic constants determined from these transitions for the X and B states of VAr^+ separately.

Table 4-13. Rotational Constants of the B-State of VAr^+

v'	B-X (cm^{-1})	B'_v
5	15623.09	0.0781
6	15695.30	0.0767
13	16104.19	0.0623
17	16272.78	0.0551
18	16306.87	0.0517
20	16368.90	0.0476
22	16420.10	0.0429

The ground state of VAr^+ has been calculated by Bauschlicher to be a $^5\Sigma^+$ with a bond length, r_e, of 2.64 Å. The bond length calculated is in perfect agreement with the experimental determination and the symmetry assignment is the same as that predicted from simple Molecular Orbital considerations. If the z-axis is taken as the bonding axis,

the z^2 orbital is expected to be highest in energy followed by the xz and yz, and finally the xy and x^2-y^2 orbitals which have no z-axis component associtated with them. Figure 4-20 shows the high-spin variant of the MO diagram of VAr^+ based on the splitting of the d-orbitals expected. Based on the diagram, a spin of 5 and a net orbital angular momentum of zero is predicted resulting in $^5\Sigma$ symmetry. Based on the ground state symmetry, the excited state symmetry has been assigned as a $^5\Pi_1$, which takes into account both the spin-allowed and perpendicular nature of the observed transitions.

Table 4-14 shows the experimentally determined bond lengths of the metal-argon cations previously and currently under investigation in our lab. Comparison of the experimentally determined VAr^+, $NbAr^+$, $ZrAr^+$ and $CoAr^+$ and $NiAr^+$ bond lengths with those of different levels of theory suggests that both modified coupled pair functional (MCPF) and all-electron relativistic Dirac-Fock-Slater self-consistent-field calculations (DFS) predict bond lengths fairly well.

A single transition of the a-state of $NbAr^+$,v' =4, has also been resolved rotationally and fit to Equation 4-6. The spectrum and fit are shown in Figure 4-21, where the points represent experimental data and the solid line the fit to Equation 4-6. This electronic transition is

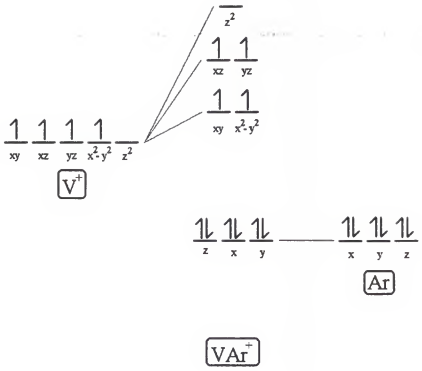

Figure 4-20. Molecular Orbital Diagram of the Ground State of VAr^+

The Molecular Orbital diagram of the ground state of VAr^+ assuming bonding along the z-axis. The total spin (5) and orbital angular momentum (0) support the $^5\Sigma$ symmetry assigned.

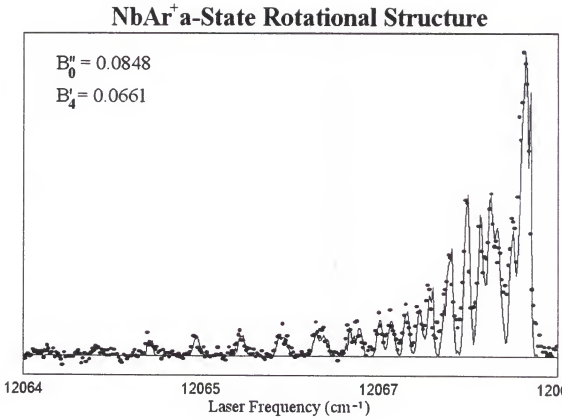

Figure 4-21. Rotational Fit of the (4,0) a-X Transition in $NbAr^+$

Experimental data points are shown by (•) and the area defined by these points, which make up the experimental contour , has been shaded grey. The single line is an instrument function superimposed upon the calculated rotational line positions calculated from Equation 4-6. The ground and excited state rotational constants shown correspond to bond lengths of 2.67 and 3.02 Å respectively.

Table 4-14. Bond Lengths and Dissociation Energies of Selected M^+·Ar Complexes
[Literature references in square brackets]

	r_0'' Experiment (Å)	r_0'' Theory (Å)
VAr^+	2.64 ± 0.01 [this work]	2.65 [35]
$NbAr^+$	2.67 ± 0.02 [a]	-
$ZrAr^+$	2.72 ± 0.01 [10]	-
$CoAr^+$	2.385 ± 0.005 [6]	2.44 [35] 2.44 [36] 2.66 [37]
$NiAr^+$	short[b]	2.38 [35] 2.42 [36] 2.59 [37]

[a] preliminary result, work in progress
[b] work currently in progress

perpendicular, involving a change in the electronic angular momentum Ω (Hunds case (c)) from Ω"= 0 in the ground state to Ω'= 1 in the excited state. The ground state bond length (v"= 0 of the ground state) has been determined to be 2.67 Å, only slightly longer than that of the VAr^+. The bond length of the v'= 4 level of the excited state is 3.02 Å.

Parameterization of VAr^+ B-State Potential Energy Surface

Since both rotational and vibrational information on the upper state of this system are now known, the interparticle potential energy function of this molecule in

the Born-Oppenheimer approximation may be investigated. A popular potential choice of a simple analytic form for the potential is the so called Morse function [38]

$$V(r) = D_e \left[1 - e^{-\beta(r-r_e)} \right]^2 \qquad (4\text{-}7)$$

The three adjustable parameters of this function are to be determined by examination of the observed (experimental) properties of the molecule. For instance, r_e is determined from the rotational constant:

$$r_e = \sqrt{\frac{h}{8\pi^2 B_e \mu c}} \qquad (4\text{-}8)$$

If the vibrational structure near the bottom of the potential is used to determine ω_e and $\omega_e x_e$, then D_e may be calculated from those two factors [39]:

$$D_e = \frac{\omega_e^2}{4(\omega_e x_e)} \qquad (4\text{-}9)$$

The final parameter needed for the Morse function, β, is determined directly from the aforementioned experimental anharmonicity:

$$\beta = \sqrt{\frac{8(\omega_e x_e)\pi^2 \mu c}{h}} \qquad (4\text{-}10)$$

Let us call the potential constructed in this way potential (1). Potential (1) should describe the actual interparticle potential well near the bottom, since the experimentally determined properties used are sensitive to that region. However, the dissociation limit of this potential is too low, 7% lower than that experimentally observed.

A second potential may be constructed using experimental values of B_e, ω_e, and D_e to fix the parameters r_e, and β (D_e is given). Call this function potential (2). It, of course has an accurate well depth, but fails to accurately predict the vibrational energy levels over most of the middle of the bound energy region. This is because the first order anharmonicity has been artificially reduced to increase the well depth. Therefore, fewer bound levels are found in this potential than the actual molecular potential supports, and the vibrational energy of every bound state is overestimated.

A Morse-type potential has a simple analytic form for the vibrational dependence of the rotational constant, or vibration-rotation coupling constant, α_e. The constant,

α_e, is determined analytically [40] from the values of B_e, ω_e, and $\omega_e x_e$ as:

$$\alpha_e = \left(\frac{6}{\omega_e}\right)\left[\left((\omega_e x_e)B_e^{\,3}\right)^{1/2} - B_e^{\,2}\right] \qquad (4\text{-}11)$$

Neither potential (1) nor potential (2) predict the rotation-vibration coupling constant, α_e, accurately for this ion state. In fact, we conclude that no Morse function can adequately describe all the spectroscopic constants of the B state of VAr^+ or any state of an ionic molecule from equilibrium to dissociation. The functional form, although popular, does not have the correct long-ranged behavior ubiquitous in ionic potentials. A summary of the constants derived for these potentials is given in Table 5-15.

Now that the Morse potential has been shown not to describe the B-state of VAr^+, we turn to a second popular choice of a potential energy function, the Born-Mayer. The Born-Mayer potential includes both a repulsive exponential and attractive terms of the form $1/r^n$. We have chosen a Born-Mayer potential with the form [41]:

$$U(r) = be^{-r/\rho} - \frac{C}{r^4} - \frac{E}{r^6} \qquad (4\text{-}12)$$

Table 4-15. Comparison of Morse Functions for the $^5\Pi_1$ B State of VAr^+

Potential	(1)	(2)	Actual
Input	r_e, ω_e, $\omega_e x_e$	r_e, ω_e, D_e	-
v_D[a] vib	28.5	30.6	48.8[c]
v_D[b] rot	52.4	55.0	43.2[d]
r_e [Å]	(2.89)	(2.89)	2.89
ω_e [cm^{-1}]	(90.4)	(90.4)	90.4
$\omega_e x_e$ [cm^{-1}]	(1.56)	1.45	1.56
D_e [cm^{-1}]	1309	(1407)	1407
α_e x 10^3 [cm^{-1}]	1.70	1.62	2.06
β [$Å^{-1}$]	1.44	1.39	-

[a] The vibrational quantum number at which $\Delta G(v)$ becomes negative.

[b] The vibrational quantum number at which the rotational constant is zero.

[c] Determined from a Leroy Bernstein analysis of near dissociation vibrational structure, see ref [1].

[d] Determined from the vibrational dependence of the bond length.

where the $1/r^4$ term represents the charge-(induced dipole) and the $1/r^6$ term accounts for the charge-(induced quadrapole) and dispersional forces. A potential of the form given in Equation 4-12 will be refered to for the remainder of this discussion as a BM[exp,4,6] potential. The four parameter potential (b, ρ, C, E)has been chosen so as to fit the experimental determined constants r_e, $w_e x_e$, D_e and α_e. The coeffecient of the charge-(induced dipole) term, C is defined by Equation 4-3. The additional parameters may be determined by relations involving Equation

3-12 and its first and second derivative. By definition, Equation 3-12 is equal to the dissociation energy at r_e,

$$U(r_e) = be^{-r_e/\rho} - \frac{C}{r_e^4} - \frac{E}{r_e^6} = D_e \tag{4-13}$$

while the first derivative is equal to zero at r_e,

$$U'(r_e) = -\frac{b}{\rho}e^{-r_e/\rho} + \frac{4C}{r_e^5} + \frac{6E}{r_e^7} = 0 \tag{4-14}$$

and the second derivative is equal to the force constant K at r_e.

$$U''(r_e) = \frac{b}{\rho^2}e^{-r_e/\rho} - \frac{20C}{r_e^6} - \frac{42E}{r_e^8} = K \tag{4-15}$$

By manipulation of Equations 4-13 through 4-15, the exponential can be eliminated and expressions for b and ρ, solved in terms of the constant C and E, can be derived. By solving Equations 4-13 and 4-14 for the exponetial and equating the resulting equations the constant ρ is found to be:

$$\rho = \frac{\frac{C}{r_e^4} + \frac{E}{r_e^6} - D_e}{\frac{4C}{r_e^5} + \frac{6E}{r_e^7}} \qquad (4\text{-}16)$$

The expressions for b can then be found by rearrangement of Equation 4-14:

$$b = e^{r/\rho}\,\rho\left[\frac{4C}{r_e^5} + \frac{6E}{r_e^7}\right] \qquad (4\text{-}17)$$

The parameter C is of course fixed by the polarizability of argon, and E is an adjustable parameter used to restrain r_e to the experimental value of 2.89Å. Table 4-15 contains the optimized BM[exp,4,6] parameters which have been found to best represent the B-state of VAr^+. Figure 4-22 shows both the BM[exp,4,6] potential and a BM[exp,4] potential. The BM[exp,4] potential is equivelent to setting E=0 in Equations 4-12 through 4-16 and the optimized parameters appear in Table 4-15. It is clear that the BM[exp,4]potential does not predict the equilibrium bond length correctly, and suggested the addition of the $1/r^6$ term. Thusfar, the parameterized BM[exp,4,6] potential predicts both the correct dissociation energy and equilibrium bond length. In order to verify that that the vibrational and rotational eigenvalues of the B-state are replicated, the turning points of the potential must first

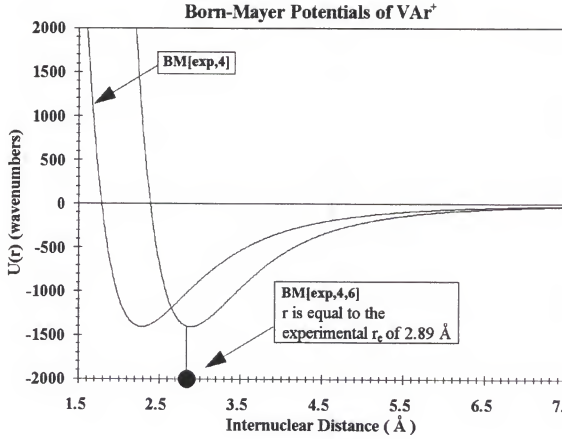

Figure 4-22. Born-Mayer Potential of the B-State of VAr^+

The BM[exp,4,6] and BM[exp,4] potentials resulting from the parameterization of the experimentally determined spectroscopic constants of Table 4-1. The parameters utilized to generate the two potentials are given in Table 4-15. The BM[exp,4] potential does not replicate the correct equilibrium bond length, which suggested the addition of a $1/r^6$ attractive term.

be approximated. Turning points are the two internuclear distances and energies which define the repulsive and attractive side of each vibrational level of the potential. To determine the turning points the well known Wentzel, Kramers and Brillouin (WKB) method [42]was used.

The WKB method is a semiclassical method which relates the potential energy, U(r), of a diatomic system to the vibrational index, v, through Equation 4-18. The

$$(2\mu)^{1/2} \int [E(v) - U(r)]^{1/2} dr = h\,(v+\frac{1}{2}) \qquad (4\text{-}18)$$

vibrational eigenvalues which quantize the integral can be approximated numerically and a program written in C, called WKB, has been develped for this purpose.

The estimated turning points for the B-state of VAr^+ were then input into program LEVEL [43], which joins the turning points through a cubic spline, and uses a $1/r^4$ attractive term to extrapolate the long range portion of the potential to the dissociation limit. For the potential in the region which is lower in energy than the first three sets of turning points, an exponential is fitted inward. The eigenvalues for the potential, including the rotational constants B_v, are then calculated by solving the one-

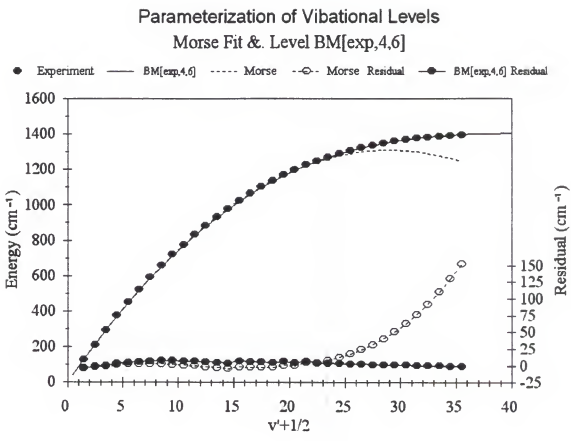

Figure 4-23. Comparison of the Vibrational Energy Levels Predicted by the Morse and Level BM[exp,4,6] Fits to Experimental Transition Frequencies

The vibrational energy levels predicted by the Level analysis of the BM[exp,4,6] potential and the Morse Fit using Equation 4-1 are compared to the experimental VAr* B-X transition frequencies . The dashed-line represents the morse fit, which predicts the incorrect dissociation energy, but accurately describes the lower vibrational structrure. The BM[exp,4,6] potential predicts the correct dissociation energy and the residuals to the experimental transition frequencies indicate the vibrational structure to be well described throughout the potential.

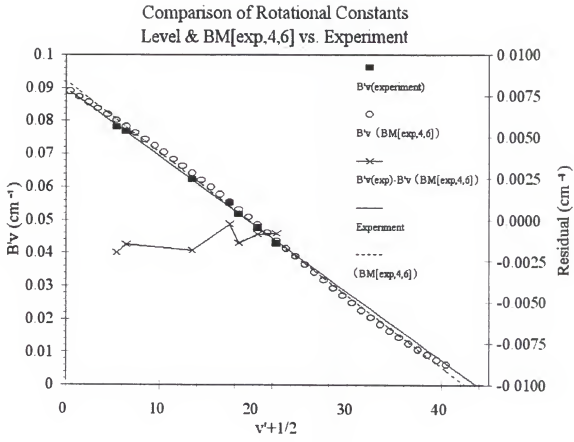

Figure 4-24. Comparison of the Level BM[exp,4,6] Rotational Constants to Experiment

The experimentally derived rotational constants, resulting from the fits of the rotationally resolved bands of the B-State of VAr^+, are compared to those calculated by Level and the BM[exp,4,6] potential. The residuals to the calculated experimental rotational constants show the BM[exp,4,6] potential to adequately describe the rovibronic structure, including the equilibrium bond length and vibration-rotation coupling constant.

dimensional Schrödinger equation. For futhur details of the procedures implemented in Program LEVEL, the reader is refered to reference [43].

Table 4-16. Parameters of and Constants Calculated from the Born-Mayer Potentials of the B-State of VAr^+

	BM[exp,4,6] Parameter	BM[exp,4] Parameter
r_e (Å)	2.89	2.29
D_e (cm^{-1})	1407	1407
α ($Å^3$)	1.49	1.49
b (cm^{-1})	1.54×10^7	2.43×10^6
ρ (Å)	0.324	0.316
C ($Å^4$ cm^{-1})	8.58×10^4	8.58×10^4
E ($Å^6$ cm^{-1})	1.29×10^6	0
α_e	2.17×10^{-3}	-
v_D	42.5	-

Figures 4-23 and 4-24 show the comparison of the LEVEL determined eigenvalues for the B-state of VAr^+ to those experimentally determined. For comparsion in Figure 4-23, the Morse Fit using Potential (1) and constants of Table 4-15 are included. The BM[exp,4,6] potential fits the vibrational eigenvalues quite well, even in the vicinity of the dissociation limit where the Morse is observed to deviate substantially. Likewise, the experimental rotational constants are predicted fairly accurately as is

the vibration-rotation coupling constant, α_e. The number of bound vibrational levels predicted by the LEVEL vibrational and rotational analysis is self-consistent, predicting v_D= 42.5, which is lower than that determined by LB-Analysis, v_D = 48.8. A summary of the the parameters and molecular constants calculated from the Born-Mayer type potentials appears in Table 4-16.

Qualitiative Trends in the Photodissociation Spectra

Through comparison of the the photodissociation spectra shown in Figures 4-1 through 4-6 a few general trends may be identified. When the polarizability of the ligand increases (Ar< Kr< Xe) and the metal cation remains constant a blue shift in the band origin is observed. This is most easily seen through comparison of the B-states of VAr^+, VKr^+ and VXe^+, and the B-states of $NbAr^+$ and $NbXe^+$. On the contrary, a large red shift in band origin is observed when the metal cation is changed from V^+ to Nb^+ and the neutral ligand remains unchanged. The red-shift is obvious from comparison of the B-states of VAr^+ and $NbAr^+$, and the B-states of VXe^+ and $NbXe^+$. The shift results from the decreased atomic energy of analogous metal cation atomic states as the size of the metal increases. The same shift

in band origins is not as easily observed in $TaAr^+$ due to the change in ground state metal electron configuration from nd^4, for both V^+ and Nb^+, to $5d^3\ 6s^1$ for Ta^+. To facilitate identification and prediction of the dissociation limits thusfar unassigned, Figure 4-25 shows a correlation diagram of selected electronic states of V^+, Nb^+ and Ta^+. The atomic energies utilized originate from reference [31].

Another observation can be made through comparison of the spectra of VAr^+ and $NbAr^+$ in the region of the dissociation limit of the B-states. In VAr^+ the B-state dissociation limit leads into a region of increased non-resonant photodissociation, evident in the increased baseline, and the end of B'-state structure. In $NbAr^+$, the B-State dissociation limit shows a similar increase in non-resonant photodissociation, but the b-X transitions ride upon it. Although it is suprising that a spin-forbidden transition, which typically is of lower intensity than a spin-allowed, carries through the B-state limit, a plausible explanation can be made. First, the intensities of the B'-X transitions appear to be relatively small and of rapidly diminishing intensity, possibly due to poor Frank-Condon overlap, as the B-state limit is approached. Second, the increased spin-orbit coupling present in $NbAr^+$ vs. VAr^+, which results from the increased atomic number of Nb, causes

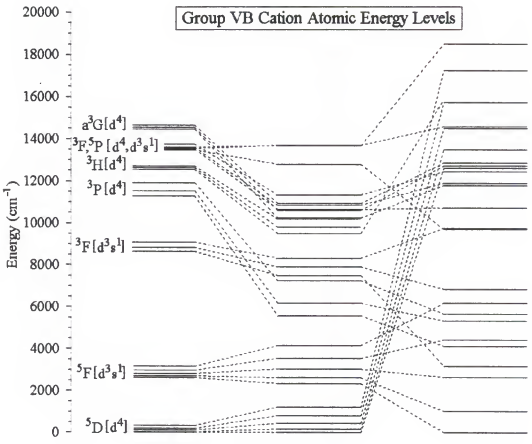

Figure 4-25. Correlation Diagram of the Group VB Atomic Energy Levels

The energy levels of selected atomic states of the Group VB transition metals are shown. Through the differences in energy of common atomic terms the expected dissociation limits of electronic states not observed for one complex may be predicted from another.

the $\Delta S=0$ selection rule to hold less strictly, increasing the intensity of the transition.

Trends in Binding Energy

To facilitate the discussion of observed trends in binding energy, selected ground and excited state dissociation energies appear in Table 4-16. As one would expect from the charge-(induced dipole) nature of the attraction, the binding energies of the excited and ground states increase with the polarizability of the rare gas when the metal cation remains unchanged. When Group VB is descended and the neutral remains unchanged the excited states of the complexes of V^+ and Nb^+ with rare gas ligands experience a decrease in binding energy while the ground states exhibit the opposite trend and become more bound. The decrease in binding energy of the excited states has been attributed to the increased radial size of the metal cation which results from the s-orbital occupation in the excited state. The increased electron density along the bonding axis due to s-orbital occupation shields the neutral ligand from the charge-(induced dipole) attraction reducing the binding energy. The slight increase in binding energy of the ground states of the vanadium and niobium cationic

Table 4-17. Selected Experimental Binding Energies of Group VB Rare Gas Cations

	D_0'	D_0''
VAr^+	1361 $\{3d^3\ 4s^1\}$	2982 $\{3d^4\}$
VKr^+	2057 $\{3d^3\ 4s^1\}$	3830 $\{3d^4\}$
VXe^+	3220 $\{3d^3\ 4s^1\}$	5240 $\{3d^4\}$
$NbAr^+$	1243 $\{3d^3\ 4s^1\}$	3106 $\{4d^4\}$
$NbXe^+$	3051 $\{4d^3\ 5s^1\}$	5815 $\{4d^4\}$
$TaAr^+$	888 $\{5d^3\ 6s^1\}$	1661 $\{5d^3\ 6s^1\}$

complexes is suprising. From the rotational analysis of VAr^+ and $NbAr^+$ presented earlier, Nb^+ is 0.06 Å larger than V^+ and would therefore be expected to have a slightly smaller binding energy. Calculations have suggested that transition metal cations can reduce metal-ligand repulsion by changing the orientation of the d-orbitals, allowing the neutral closer and increasing the charge-(induced dipole) attraction [44]. It may be that as radial size of the cation increases, the energetic cost of such a rearrangement decreases, allowing for a closer cation-neutral association and the unexpected trend in ground state binding energy.

The complexes of Ta^+ are unique in that the ground state of Ta^+ has an occupied s-orbital. It is the change in ground state electron configuration which is responsible for the relatively weak binding energy of $TaAr^+$ as compared to VAr^+ and $NbAr^+$. The s-orbital occupation of the ground

state increases the electron density along the bonding axis and decreases the charge-(induced dipole) attraction. The excited states of $TaAr^+$ observed are less bound than the ground state, as evidenced by the red-degraded nature of the bands, even though both $6s^15d^3$ (A and B-states) and $5d^4$ (C-state) configurations are observed.

Comparison to Theoretical Calculations

Very few transition metal-rare gas diatomic cations other than those presented here have been studied experimentally or theoretically. Table 4-17 lists the known ground state experimental and calculated binding energies and the error present in the calculated values. The only Group VB complex which has been both experimentally and theoretically investigated is VAr^+. The binding energy is predicted to be 15.3% lower than our experimental determination, while the excited $^5\Pi$ state (not shown in Table 3-18) is calculated to be 1759 cm^{-1}, 25% too high. The roughly 20% average error is typical of the calculation employed given that the same relative error is observed when similar comparisons are made to other charge-(induced dipole) metal cations. It is obvious from Table 4-17 that modern theoretical methods are not yet capable of accurate

calculation of binding energies for even the smaller inductively bound systems.

Table 4-18. Ground State Dissociation Energies of Selected Transition Metal Cation-Argon Complexes [Literature references in square brackets]

	D_0" Experiment (cm^{-1})	D_0" Theory (cm^{-1})	% error
VAr^+	2982 ± 10	2524[35]	-15.3%
$NbAr^+$	3106 ± 10	-	-
TaAr+	1661 ± 15	-	-
$ZrAr^+$	2706 ± 20 [10]	-	-
$CoAr^+$	4111 ± 5 [6]	3460 [35] 4298 [36] 1380 [37]	-15.8% +4.5% -66.4%
$NiAr^+$	4752 ± 5 [45]	3629 [35] 4194 [36] 1800[37]	-23.6% -11.7% -62.1%
$SrAr^+$	803 ± 244 [46]	-	-
FeAr+	-	1217 [37] 2468 [schwartz,JCP 1995]	-
$CrAr^+$	2339 [47]	887 [37] 1872 [18]	-62.1% -20.0%
$MnAr^+$	-	363 [37]	-
$CuAr^+$	-	605 [37]	-
$FeKr^+$	-	2509 [48]	-
$FeXe^+$	-	2613 [48]	

Conclusions

From the photodissociation spectra of inductively bound Group VB metal-rare gas cations, ground and excited spectroscopic constants have been determined. The origins of the observed bands are observed to undergo a blue-shift as a function of ligand size (and polarizability) when the metal ion remains the same. When the ligand remains the same and the metal is varied, equivalent excited states shift as a function of the atomic energy of the metal cation into which the complex dissociates. Binding energies of the ground and excited states have been observed to increase as a function of the polarizability of the rare gas in both the ground and excited states. The Binding energies of the excited states of V^+ and Nb^+ decrease as the metal atomic number increases and the neutral remains unchanged. The opposite trend is observed for the ground state binding energies, and has been attributed to a decreased cost of d-orbital rearrangement. From the spectroscopic constants of the B-state of VAr^+, the first parameterization of the excited state potential has been completed utilizing a Born Mayer type analytic potential. The vibrational and rotational eigenvalues calculated from the Born-Mayer potential represent the experimentally determined transition frequencies and rotational constants accurately. From the

comparison of our results with calculated binding energies and bond lengths, it has been shown that such charge-(induced dipole) complexes are not yet fully accessible by current ab initio methods. It is also evident that there is a need for additional experimental benchmarks, particularly ground state bond lengths, to aid in the evolution of present day theoretical methods. It is our hope that this, our most recent addition to this area of research, will aid in the realization of this end.

CHAPTER 5
THE PHOTODISSOCIATION OF $V^+ \cdot CH_4$

The ability of certain transition-metals to adsorb molecules such as H_2 and small hydrocarbons is of some importance to the field of heterogeneous catalysis [49]. The initial step of this process involves the formation of a potentially reactive complex before dehydrogenation or subsequent elimination reactions can proceed. A number of gas phase studies have investigated the binding energies of the first and second row transition-metal atomic ions to small hydrocarbons [50], but only a few ($Fe^+ \cdot CH_4$ [51], $Co^+ \cdot CH_4$ [52,53], $Mg^+ \cdot CH_4$ [54]) have provided experimental insight into the magnitude and nature of the binding interaction of methane to a metal ion in the reactive precursor complex.

Previous investigation of the activation of methane by translationally excited V^+ has utilized a guided-ion-beam tandem mass-spectrometer configured to monitor reaction product yield as a function of reactant collision energy [50]. Collisional products were observed only at energies higher than thermal and included VH^+ and VCH_x^+ (x=1-3). Through the use of the bond enthalpies calculated from the

collisional energy dependencies, evidence for a covalently bound $[H\text{-}V\text{-}CH_3]^+$ ion was presented and estimated to be endothermic with respect to ground state (^5D) V^+ and (^1A) CH_4, by 0.5 ± 0.25 eV. There was no experimental evidence for the formation of a weakly bound $V^+ \cdot CH_4$ complex, leaving the quantitative picture of the reaction coordinate incomplete. We have been at least partially successful at creating such elusive species through the use of a laser-driven-plasma supersonic-expansion which quenches the internal energy responsible for intramolecular rearrangement or elimination reactions. The following paper presents the results of the first spectroscopic characterization of the isolated $V^+ \cdot CH_4$ complex, motivated by the significance of such simple species in the complete understanding of model catalytic processes.

Vibrational analysis

Figure 5-1 shows the spectrum of the photodissociation action $V^+ \cdot CH_4 \rightarrow V^+ + CH_4$ as a function of dissociation laser frequency in the interval from 15900 cm^{-1} to 16400 cm^{-1}. No other photofragmentation pathways are observed under these conditions. Collision-activated-dissociative processes with residual He gas in the flight tube and non-resonant photodissociation occur producing an insignificant background fragmentation. The sharp features in Figure 5-1

are representative of 17 vibronic bands observed from 15500 cm^{-1} to 17400 cm^{-1} via resonant laser photodissociation. Laser fluence dependence of the photodissociation yield is indicative that a one-photon absorption process leads to dissociation. Of the 3N-6 = 12 vibrational modes possible for this molecule, only the $V^{+}{\cdot}CH_4$ stretch is observed to give a prominent progression in the photodissociation action spectrum. The most intense features in Figure 5-1 are the result of this progression in the stretching mode while the less intense features built upon the stretch are consistent with a $V^{+}{\cdot}CH_4$ rocking motion. The weak transition at 15880 cm^{-1}, labeled by an asterisk in Figure 5-1, is due to an intense VH_2O^{+} transition [55] which contaminated the $V^{+}{\cdot}CH_4$ photodissociation signal.

A simple formula for the transition energies of a polyatomic molecule considering only cold bands and two upper state vibrational modes active [1]:

$$E(v) = \upsilon_0 + \omega'_s v'_s - x'_{ss}(v'_s)^2 + \omega'_R v'_R \qquad (5\text{-}1)$$

has been applied to the observed band positions in the $V^{+}{\cdot}CH_4$ spectrum from which the band origin, ν_o, the stretching frequency, ω_s', the diagonal stretching anharmonicity, x_{ss}', and the rocking frequency, ω_r', are

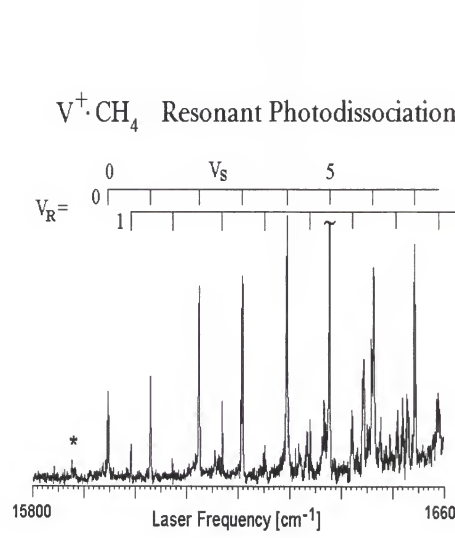

FIGURE 5-1. Photodissociation Spectrum of VCH_4^+

A portion of the resonant photodissociation spectrum of $V^+ \cdot CH_4 \rightarrow V^+ + CH_4$, i.e. relative V^+ photocurrent vs. dissociation laser frequency. The photodissociation shown results from a single absorption event. The weaker transitions evident in the spectrum originate from a $V^+ \cdot CH_4$ rock built upon the intense progression which corresponds to the $V^+ \cdot CH_4$ stretch. The labeling of the transitions corresponds to (stretch quantum number (v_s), rock quantum number (v_R)). The weak transition occuring at 15880 cm^{-1} (*) results from a broad $V^+ \cdot H_2O$ photodissociation event which contaminated the $V^+ \cdot CH_4$ photodissociation signal.

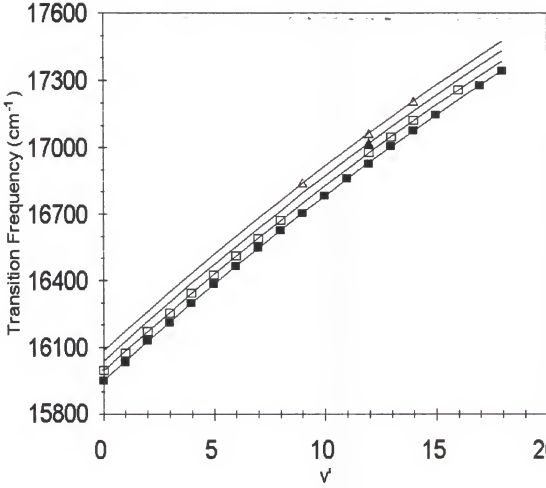

FIGURE 5-2. Fit of VCH_4' Band Positions

The least-squares fit of Equation 5-1 to the observed vibrational transitions listed in Table 5-1 (■ vibrations, □ one quanta of rock, ▲ two quanta of rock, Δ three quanta of rock). Absolute vibrational numbering is not possible due to an absence of naturally occuring isotopes of vanadium. The absolute origin corresponds to the reddest transition observed

derived. These constants are least squares fit to the observed band positions in Table 5-1 and listed in Table 5-2. In this investigation, the absence of naturally occurring minor isotopes of this molecule has made absolute vibrational nubmering via siotope shifts in the spectrum impossible. Hence the band origin is chosen by the intensity distributio absolute vibrational numbering via isotope shifts in the spectrum impossible. n in the band system to be the strong red transition at 15949.9 cm^{-1}. Figure 5-2 shows the fit of the observed transitions to Equation 5-1. The best fit in this study is obtained for the transitions $v_S' = 0 \rightarrow 18$ where ($v_S' = 1$, $v_R' = 0,1$) is not included in the least-squares regression due to a perturbation which is clearly evident in the residuals listed in Table 5-1. The lower limit to the dissociation energy of the excited state, D_0', listed in Table 2 has been estimated through a Birge-Sponer extrapolation, i.e. $D_0 \approx \omega_S^2/4x_{SS}$. A more precise determination of dissociation energy, such as a Leroy-Bernstein analysis [32], can not be performed here due to an insufficient number of transitions observed which probe levels very close to the dissociation limit. The ground state dissociation energy, D_0'', is the difference between ($T_e + D_0'$) and the atomic limit of the vanadium cation $^5P_2$ state, 13594.73 cm^{-1}, into which the $V^+ \cdot CH_4$ excited state

TABLE 5-1. Frequencies of Assigned Transitions in $V^+ \cdot CH_4$

v_s'	v_r'	Transition Frequency	Obs-Calc[a]	v_s'	v_R'	Transition Frequency	Obs-Calc[a]
0	0	15950.3	0.4	12	0	16926.2	-2.7
0	1	15995.7	1.1	12	1	16974.3	0.7
1	0	16033.8	-5.4	12	2	17018.8	0.4
1	1	16076.6	-7.4	12	3	17062.8	-0.4
2	0	16128.1	1.0	13	0	17002.9	1.6
2	1	16173.0	1.2	13	1	17046.2	0.1
3	0	16212.7	-0.8	14	0	17073.6	1.2
3	1	16255.1	-3.2	14	1	17118.1	0.9
4	0	16298.7	0.1	14	3	17206.1	-0.7
4	1	16343.5	0.1	15	0	17141.6	-0.6
5	0	16381.5	-0.8	16	1	17255.1	-0.1
5	1	16424.8	-2.3	17	0	17276.5	-0.8
6	0	16464.3	-0.3	18	0	17342.5	-0.3
6	1	16510.1	0.7				
7	0	16546.4	0.9				
7	1	16590.1	-0.2				
8	0	16623.9	-1.0				
8	1	16672.2	2.5				
9	0	16702.9	-0.2				
9	3	16837.6	0.3				
10	0	16779.4	-0.3				
11	0	16856.6	1.5				

[a]Observed minus calculated frequency from Equation (1)

diabatically dissociates. The identity of the fragment states at the diabatic disscoiation limit is assumed to be analogous to that previously determined from the photodissociation of inductively bound VAr^+[27], VKr^+[27], and VXe^+[29] which have ligand polarizabilities, stretching frequencies, and electronic structure similar to that of $V^+ \cdot CH_4$.

Table 5-2. Molecular constants of $V^+ \cdot CH_4$ (cm^{-1})

	Excited State ($3d^3\ 4s$)	Ground State ($3d^4$)
ν_o	15949.9	...
W_s	90.0	...
W_R	44.8	...
x_{ss}	0.70	...
D_o	2900±300[a]	5250±300[b]

[a] Birge-Sponer approximation
[b] (ν_o + excited state D_o) - ($^5P_2$ atomic state energy)

Discussion

The VCH_4^+ ion probably has at least two stable isomers: an inductively bound complex similar to those formed with the noble gases, $V^+ \cdot CH_4$,and a more strongly bound covalent species, $[H\text{-}V\text{-}CH_3]^+$. The ion source in this study is optimized for the 'gentle' formation of electrostatic species and it is this isomer that is expected to be the major component of the VCH_4^+ ensemble. No evidence for the formation of VH^+ or VCH_x^+(x=1-3) was observed in the nascent ion distribution, suggesting that the source conditions were too mild to induce significant high-temperature reactions, as expected. In addition, the nature of the observed photofragmentation of VCH_4^+ and its analogy to other

electrostatic complexes of V^+ indicates that the carrier of the resonant features in Figure 5-1 is indeed the electrostatically bound isomer of $V^+ \cdot CH_4$. This does not preclude the formation of a minor amount of the inserted isomer in the beam, since its optical properties are expected to be quite different from the electrostatic complex and may in fact be 'transparent' at these red wavelengths. What is clear, however, is the fact that the $V^+ \cdot CH_4$ isomer is stable and has been spectroscopically characterized for the first time in this work.

Presently, we are aware of no *ab initio* calculations of the properties of the $V^+ \cdot CH_4$ complex. However, Blomberg [56] has calculated the binding energy of methane to M^+ ions of the second transition series including isoelectronic $Nb^+ \cdot CH_4$. The SCF level calculations included correlation effects and a correction factor which compensated for the systematic underestimation in binding energy. The correction factor was determined through comparison to the binding energies of $Fe^+ \cdot CH_4$ [51], derived from the kinetic energy dependencies of collisionally induced dissociation, and $Co^+ \cdot CH_4$ [52] determined through equilibrium methods. The corrected binding energy of 6224 cm^{-1} assumes η^2-coordination (C_{2v} symmetry) of the undistorted methane ligand at a Nb^+-C bond distance of 2.65 Å. Utilizing the

calculated 0.7 units of charge localized on the metal, the total charge-induced-dipole attraction amounts to ~24% of the binding. Unfortunately, our investigation can not validate the C_{2v} symmetry of the ion nor the breakdown of the electrostatic contributions to the binding energy until rotational analysis of the spectrum is completed. However, the $V^+ \cdot CH_4$ ground state binding energy is slightly less than that calculated by Blomberg which is in accord with relative binding trend in argon complexes of the same two metals.

The experimental dissociation energies of the methane bound first-row transition metal ions previously investigated are listed in Table 5-3. $Fe^+ \cdot CH_4$, having a $4s^13d^6$ electron configuration, is the least bound due to the repulsive interaction between the singly occupied 4s orbital with the methane ligand. The ground state configurations of the vanadium and cobalt ions are $3d^4$ and $3d^8$, respectively, with no s-orbital occupation. Thus, s-orbital occupancy on the metal ion has the effect of reducing the electrostatic binding as can be seen in the increased binding energy of the ground state relative to the excited state of $V^+ \cdot CH_4$. The effect of d-orbital contraction is seen in the decrease in bond strength of $V^+ \cdot CH_4$ relative to that of $Co^+ \cdot CH_4$.

Table 5-3. First-Row ground state $M^+ \cdot CH_4$ binding energies

	configuration	cm^{-1}
$V^+ \cdot CH_4$	$3d^4$	5250±300[a]
$V^+ \cdot CH_4$	$3d^3$ 4s	2900±300[a]
$Fe^+ \cdot CH_4$	4s $3d^6$	4791±280[b]
$Co^+ \cdot CH_4$	$3d^8$	8008±480[c]

[a] This work
[b] Reference [3]
[c] Reference [4]

Conclusions

The electronic spectrum of $V^+ \cdot CH_4$ has been probed spectroscopically via single-photon resonant photodissociation for the first time. The vibrational structure has been analyzed to yield the $V^+ \cdot CH_4$ stretching and rocking frequencies in addition to the diagonal stretch-stretch anharmonicity of the excited state. The dissociation energy of the excited state is lower than that of the ground state which is consistent with increased electronic repulsion along the bonding axis associated with the occupied 4s oribtal. Although $V^+ \cdot CH_4$ is representative of one of the simplest forms of a hydrocarbon bound to a metal ion, the binding interaction is highly complex and only through accurate rotational analysis will the questions concerning the individual contributions be understood. It is our hope that the molecular constants and binding energy determined will prove valuable to the elucidation of the

energetics and mechanisms responsible for metal ion mediated reactions.

CHAPTER 6
THE BOND LENGTH OF CoO^+

Interest in the structure and reactivity of small cationic transition metal oxides has increased over the last few years resulting in a number of theoretical investigations. Of particular interest have been the late first-row transition metal oxides, specifically FeO^+[57,58,59,60], CoO^+[57,59,60], NiO^+[57,59,60], and CuO^+[57,59,60] due to their ability to react with dihydrogen and both saturated and unsaturated alkanes. The early transition metal oxides ScO^+, TiO^+, VO^+, CrO^+, and MnO^+[59,60] have also been investigated but have been found to be relatively inert and therefore of less interest as oxidation agents. The aforementioned theoretical investigations have suggested ground state bond lengths and symmetries, but no experimental verification for the spectroscopic constants reported or symmetry assignment has surfaced. Experimental verification is of particular importance when conflicts arise between theoretical studies. For example, CoO^+ has been characterized by Goddard [61], who assigns the ground state symmetry as $^3\Sigma_g^-$, while both Schwarz [57], and Bauschlicher [60] have assigned the ground state to $^5\Delta$. The rotational analysis presented here supports the $^5\Delta$

assignment of the ground state of CoO^+, and provides accurate ground and excited state spectrometric constants.

Rotational Analysis

Figure 6-1 shows a single band of the A-X system of isolated CoO^+. The figure is labeled using a Hund's Case C designation, where the two state designations involved in the transition (A for the excited state, X for the ground state), is followed by the [transition origin], and total electronic angular momentum, $\Omega = \Sigma+\Lambda$, following each origin. The experimental spectrum and simulated rotational contours (details of which are given in Chapter 3) based on the ground state electronic angular momentum proposed by Goddard (lower simulation Figure 6-1) and Schwarz and Bauschlicher (upper simulation Figure 6-1) are shown. Based upon the situation, the A-X transition is perpendicular, involving a change in the electronic angular momentum from $\Omega''= 4$ in the ground state to $\Omega'= 5$ in the excited state. The simulation of the partially resolved rotational structure for the three bands we have observed gives a consistent rotational constant of $B_0''= 0.4962\ cm^{-1}$ ($r_o''= 1.6429 \pm 0.0017$) for the $v''=0$ level of the X-state. The excited state rotational constants vary linearly with v'

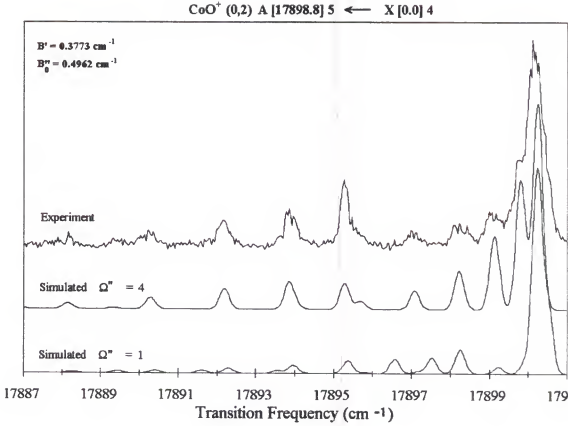

Figure 6-1. Fit to the (0,2) Band of the A-State of CoO^+

The rotationally resolved photodissociation spectrum of the (0,2) band of CoO^+ is shown while the simulated contours of the fit line positions assume $\Omega'' = 1$ or 4. Based on the simulations, $\Omega''= 4$ best represents the observed line-positions and branch structure.

which can be seen in the decrease of $B_0' = 0.3867$ cm^{-1} (Table 6-1) to $B_2' = 0.3773$ cm^{-1} (Table 6-1).

Table 6-1 Transition Frequencies and Rotational Constants of the A-State of CoO

Band Origin	(v',v'')	B_v'	r_v'
16712.5	(0,0)	0.3867	1.8610
17310.9	(0,1)	0.3806	1.8759
17898.8	(0,2)	0.3773	1.8840

Figure 6-2 shows the vibrational dependence of the upper state rotational constants. The excited state rotational constants decrease linearly with v' and are listed in Table 6-1. The vibrational numbering given in Table 6-1 is not absolute. Accurate determination of the vibrational numbering via isotope analysis was not possible due to a lack of naturally occurring isotopes of either cobalt or oxygen atoms in an abundance sufficiently large to detect in our mass spectrometer. The excited state vibration-rotation constant, α_e', has been determined to be $(4.7\pm0.3) \times 10^{-3}$ cm^{-1}. Extrapolating the dependence to the ordinate axis yields a rotational constant at the equilibrium position of the excited state potential of $B_e' = 0.3909$ cm^{-1} which corresponds to a bond length of 1.85 Å. The vibrationless or zero-point level of the same excited state, r_0, is slightly longer due to the

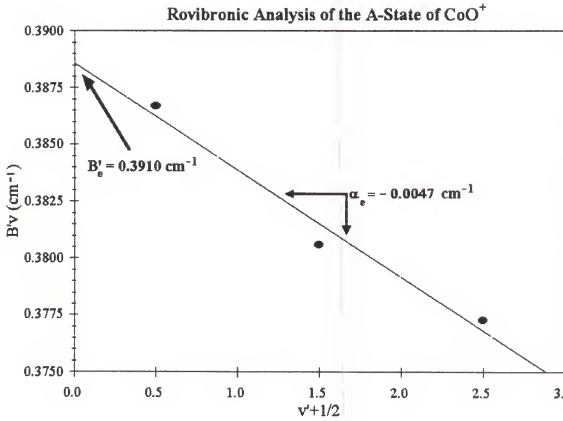

Figure 6-2. Vibrational Dependence of the A-State Rotational Constants

The vibrational dependence of the A-State rotational constants is shown. The slope of the plot gives the vibration-rotation coupling constant, α_e, while the intercept with the ordinate axis provides the rotational constant (and bond length) at the equilibrium position of the potential.

anharmonicity of the potential surface, and is found to be 1.86 ±0.01 Å. Table 6-2 lists the complete set of experimentally determined molecular constants for the ground and A-state of CoO^+.

Table 6-2 Spectroscopic Constants of CoO^+

	Symmetry	B_o (cm^{-1})	r_o (Å)	α_e (cm^{-1})	$\Delta G(v)$
A-State	-	0.3886 ±0.0010	1.8565 ±0.0017	-0.0047 ±0.001	~700 cm^{-1}
X-State	$^5\Delta_4$	0.4962 ±0.0010	1.6429 ±0.0017	-	-

Discussion

From the rotational structure evident in Figure 6-1, it is clear that there is a definite separation between the head in the R-branch (17900.2 cm^{-1}) and the beginning of the Q branch (17894.6 cm^{-1}). This branch gap is typical of a transition from a ground state having unquenched electronic angular momentum. The simulation which utilized an Ω'' of 1 failed to duplicate the branch separation and introduced rotational transitions into the simulation which are not present in the experimental spectrum. These spurious transitions are forbidden in the $\Omega''=4$ simulation, as J'' must be larger than or equal to the projection of J'' onto the internuclear axis, Ω''. Although neither Σ or Λ are good

quantum numbers in Hund's Case C, the Ω"=4 simulation supports the Hund's Case A symmetry assignment of $^5\Delta_4$ (Ω" = Σ+Λ = 2+2 = 4), proposed by both Bauschlicher and Schwarz for the ground state of CoO^+, and disputes the $^3\Sigma_1$ proposed by Goddard. Schwarz does predict a low-lying $^3\Sigma_1$ excited state [57] which is approximately 1.0 eV above the $^5\Delta$ and results from movement of an electron from a 3σ to a 1δ nonbonding orbital.

Table 6-3 Selected Spectrometric Parameters of CoO^+, CoO, and FeO

	Symmetry	B'' (cm^{-1})	r'' (Å)	[Reference] and Method
CoO^+	$^5\Delta_4$	0.4962 [a]	1.6429 [a]	this work
	$^5\Delta$	0.4968 [b]	1.642 [b]	[60] Calculation
	$^5\Delta$	0.510 [b]	1.62 [b]	[57] Calculation
CoO	$^4\Delta$	0.5037 [a]	1.631 [a]	[62] Experiment
	$^4\Delta$	0.5271 [b]	1.594 [b]	[63] Calculation
FeO	$^5\Delta$	0.5109 [a]	1.6283 [a]	[64] Experiment
	$^5\Delta$	0.5024 [b]	1.642 [b]	[63] Calculation

[a] With respect to the vibrationless level, ie. v''=0.
[b] With respect to the equilibrium position of potential.

Table 6-3 lists the rotational constants and bond

lengths calculated and experimentally determined for the ground states of CoO^+, FeO which is isoelectronic with CoO^+, and CoO. The theoretical calculations predict the ground state bond lengths extremely well, the three-parameter hybrid B3LYP density functional method of Bauschlicher providing the best estimation for CoO^+. The bond lengths experimentally determined for neutral FeO and CoO are similar to eachother but both are slightly shorter than that of CoO^+.

Summary

The rotational constants, bond lengths and vibration-rotation coupling constant of CoO^+ have been determined for the A-X transitions observed from 16500-18000 cm^{-1}. The ground state symmetry suggested by Bauschlicher and Schwarz, $^5\Delta$, is supported by our analysis while the $^3\Sigma$ assignment of Goddard appears to be a low-lying excited state. The ground state bond length determined for CoO^+ is slightly longer than those of FeO and CoO.

APPENDIX
COMPUTER PROGRAMS

TOFMS Program Description

Program TOFMS is a TOF mass spectrum display and calibration program written in the c-programming language. TOFMS reads in a time-of-flight mass spectrum file generated by the experimental control routine which has been described in detail before [65]. The program utilizes a one-point calibration of the TOF data, described in Chapter 2, by placing a cursor on a known mass peak, pressing 'M', and entering the correct mass to charge ratio (m/z). The cursor position, whose position appears at the bottom of the screen, may be toggled to display m/z or time-of-arrival (TOA). After calibration the spectrum intensity and TOA axis may be manipulated and the assignment of unknown m/z peaks made by moving the cursor position. At any point a file may be generated which contains [m/z : intensity] data which can then be imported into any program capable of reading ANSI DOS delimited text. In Table A-1, the commands supported by TOFMS are listed and described.

Table A-1. Commands Supported by Program TOFMS

Command	Description
a	Automatic scaling of TOA and intensity axis
i	Input TOF Data File
c	Toggles cursor control on/off
m	Toggles display from TOA to m/z
M	Reads correct m/z at current cursor position
O	Outputs the TOF Data to a user-specified file
w	Changes the display to black and white
x	Allows for manual timing axis scaling
y	Allows for manual scaling of m/z intensity
ESC	Quits program TOFMS
UPARROW	Increase intensity scale
DOWNARROW	Decrease intensity scale
LEFTARROW	Shifts mass spectrum left
RIGHTARROW	Shifts mass spectrum right
CTRL RIGHTARROW	Shifts mass spectrum right by a larger shift than RIGHTARROW
CTRL LEFTARROW	Shifts mass spectrum left by a larger shift than LEFTARROW
ALT RIGHTARROW	Shifts mass spectrum right by a larger step size than CTRL RIGHTARROW
ALT LEFTARROW	Shifts mass spectrum left by a larger step size than CTRL LEFTARROW
F9	Moves cursor position to left
F10	Moves cursor position to right
CTRL F9	Moves cursor position left by a larger step size than F9
CTRL F10	Moves cursor position right by a larger step size than F10
ALT F9	Moves cursor position left by a larger step size than CTRL F9
ALT F10	Moves cursor position right by a larger step size than CTRL F10

TOFMS.C Program Code

```
/*********************************************************/
/********************** Program TOFMS.c ******************/
/******************** Last Revised 5/25/97 ***************/
/******** Written by and Thomas Hayes & P. J. Brucat ******/
/************** Adapted From Program Scncmp3d.c ***********/
/*********************************************************/

#define LINT_ARGS
#include <pjb.h>
#include "keys_c.h"
#define HEADLN "TOFMS Data Calibration and Display 5/25/97
     PJB/TWH\n"
#define CALIB "To calibrate place the cursor on a peak,
     press 'M'\n"
#define CALIBR "and enter the value of the correct m/z\n"
#define graphmode() _setvideomode(_VRES16COLOR)
#define textmode() _setvideomode(_DEFAULTMODE)
#define cls() _clearscreen(_GCLEARSCREEN)
#define HRES            512         /* 640 X 480 */
#define LEFT            64
#define RIGHT           576
#define TOP             80.0
#define BOT             420.0
#define TOPBOT          -340.0      /* TOP minus BOT */
#define CURVES          3
#define TICKLEN         3.0
#define ESIZE           4000  /* max length of input file */
#define TICK_COLOR      15
#define BOX_COLOR       8
#define CURSOR_COLOR    11
#define CURVE0          12
#define CURVE1          14
#define CURVE2          13

float     vmin,
          vmax,
          iscale=1.2,
          evmin=1,
          evmax=100,
          freq_shift[CURVES],
          Massfact=1,     /*  One-Point Calibration Factor */
          cursor;
int       ebins[CURVES],
          typeout=1,
```

```
          cursor_on=1,
          active=0,
          scan=0,
int       c;
char      fnam[CURVES][80];
float huge esig[CURVES][2][ESIZE];

float line_lst[300];

/******* TOF DATA and Timing FILE INPUT *****************/

int fread_data(char *fnam, int n)
{
     FILE *dfile;
     float intensity, thetime, starttime, inctime, intscale,
           crap,a,b;
     int i,num;
     char stext[80];

     dfile = fopen(fnam,"r");
     locate(0,0);
     if(dfile == NULL) return(0);
     for(i=0;i<21;i++)
          {
               fscanf(dfile,"%*d %*s %f",&crap);
               if (i==7) {inctime=crap/1000;}
               if (i==6) {intscale=crap;}
               if (i==20) {starttime=crap/1000;}
          }
     printf("%f   %f   %f",inctime,intscale,starttime);
     skeyin(n);
     for(i=0;i<53;i++)  /* skipping to start of TOF data */
          {
               fscanf(dfile,"%*d %*s %f",&crap);
          }
     fscanf(dfile,"%*s %f",&intensity);
     esig[n][1][0]=255-(intensity/intscale);
     esig[n][0][0]=starttime;
     for(num=1;((fscanf(dfile,"%f",&intensity) != EOF) &&
     (num<ESIZE));num++)
          {
               esig[n][1][num]=255-(intensity/intscale);
               esig[n][0][num]=starttime+(num*inctime);
          }
     a=b=esig[n][1][0];
     for(i=0;i<num;i++)
          {
               if(esig[n][1][i]<a) a=esig[n][1][i];
               if(esig[n][1][i]>b) b=esig[n][1][i];
```

```
          }
     evmin=esig[n][0][0];
     evmax=esig[n][0][num-1];
     b -= a;
     for(i=0;i<num;i++)
          {
               esig[n][1][i] -= a;
               esig[n][1][i] /= b;
          }
     ebins[n]=num;
     freq_shift[n]=0.0;
     fclose(dfile);
     vmax=evmax;
     vmin=evmin;
     return(1);
}

/****************** Plots TOF Spectum ********************/

void plot_esig(int n)
{
     int i,x,y,onscale=0;
     float ehscale,fx;

     _setcolor(CURVE0);
     ehscale = (vmax-vmin);
     y = (int)(BOT + TOPBOT*esig[n][1][0]/iscale);
     if (y<TOP) y=TOP;
     if (y>BOT) y=BOT;
     fx = (float)(LEFT+
HRES*((esig[n][0][0]-vmin)/ehscale));
     if ((fx>=LEFT)&&(fx<HRES+LEFT))
          {
               x=(int)fx;
               _moveto(x,y);
               onscale=1;
          }
     for(i=1;i<ebins[n];i++)
          {
               y = (int)(BOT + TOPBOT*esig[n][1][i]/iscale);
               if (y<TOP) y=TOP;
               if (y>BOT) y=BOT;
               fx = (float)(LEFT +
               HRES*((esig[n][0][i]-vmin)/ehscale));
               if((fx>=LEFT)&&(fx<HRES+LEFT))
                    {
                         x=(int)fx;
                         if(onscale) {_lineto(x,y);}
                         else {_moveto(x,y);onscale=1;}
```

```
                    }
               else {onscale=0;}
          }
}

/************* Draws Spectrum Box and Header **************/

void box()
{
     int xt,yt;
     long itick,bigtick,medtick;
     double low,high,tick,tick_inc;
     char stext[80];

     cls();
     _settextcolor(CURVE0);
     printf(HEADLN);
     _settextcolor(CURVE1);
     printf(CALIB);
     printf(CALIBR);
     _setcolor(BOX_COLOR);
     _moveto(LEFT,(int)BOT);
     _lineto(LEFT,(int)TOP);
     _lineto(RIGHT,(int)TOP);
     _lineto(RIGHT,(int)BOT);
     _lineto(LEFT,(int)BOT);
     if(cursor_on)
          {
               _setcolor(CURSOR_COLOR);
               xt =
LEFT+(int)(HRES*(cursor-vmin)/(vmax-vmin));
               if((xt<LEFT) || (xt>RIGHT))
                    {
                         cursor = (vmin+vmax)/2.0;
                         xt = LEFT+(int)
                         (HRES*(cursor-vmin)/(vmax-vmin));
                    }
          _moveto(xt,TOP);
          _lineto(xt,BOT+15);
          _moveto(xt+1,BOT+15);
          _lineto(xt+1,BOT+10);
          _moveto(xt-1,BOT+15);
          _lineto(xt-1,BOT+10);
          }
     _setcolor(TICK_COLOR);
     if((vmax-vmin)>300.0)
          {
               tick_inc = 10.0;
               low = ((10.0*floor((double)vmin/10.0))+10.0);
```

```
            high = (10.0*floor((double)vmax/10.0));
            bigtick = 1000L;
            medtick = 500L;
        } else if((vmax-vmin)<25.0)
            {
                tick_inc = 0.2;
                low=((0.2*floor((double)vmin/0.2))+0.2);
                high = (0.2*floor((double)vmax/0.2));
                bigtick = 100L;
                medtick = 10L;
            } else
        {
            tick_inc = 2.0;
            low = ((2.0*floor((double)vmin/2.0))+2.0);
            high = (2.0*floor((double)vmax/2.0));
            bigtick = 500L;
            medtick = 100L;
        }
for(tick=low;tick<=high;tick+=tick_inc)
        {
            xt = LEFT+
            (int)(HRES*((float)tick-vmin)/(vmax-vmin));
            _moveto(xt,(int)BOT);
            yt=BOT+2*TICKLEN;
            itick = (long)(tick*10.0);
            if(!(itick%bigtick)) yt=BOT+4*TICKLEN;
            else if(itick%medtick) yt=BOT+TICKLEN;
            _lineto(xt,yt);
        }
_settextcolor(CURVE0);
_settextposition(5,0);
sprintf(stext,"FILE: %s",fnam[0]);_outtext(stext);
_settextposition(3,50);
locate(27,2);printf("%8.f",vmin);
locate(27,68);printf("%8.f",vmax);
if(cursor_on)
        {
            _settextcolor(CURSOR_COLOR);
            _settextposition(29,34);
            if (typeout)
                sprintf(stext,"mass=%9.2f",(Massfact*
                cursor*0.174757+0.4298364)*(Massfact*
                cursor*0.174757+0.4298364));
                _outtext(stext);
            else
                sprintf(stext,"time=%9.2f",(Massfact*
                cursor));
            _outtext(stext);
```

```
          }
}

/************* Shifts Mass/Arrival Time Axis **************/

void shift(float del, int a, int n)
{
     int i;

     if((a==0)||(a==1))
          for(i=0;i<ebins[n];i++) esig[n][a][i] += del;
}

/************** Gets Name of TOF DATA File ****************/

void in_data(int n)
{
     do
     {
          locate(6,15);
          printf("filename for input [%ld]?: ",n);
          skeyin(fnam[n]);
     } while (!fread_data(fnam[n],n));
}

/******************* Scales Intensity *********************/

void mult(float del, int a, int n)
{
     int i;

     if((a==0)||(a==1))
          for(i=0;i<ebins[n];i++) esig[n][a][i] *= del;
}

/****************** Screen Color to B&W *******************/
void black_on_white()
{
     int i;

     for(i=1;i<16;i++) _remappalette(i, _BLACK);
     _remappalette(0, _BRIGHTWHITE);
}

/************** Output TOF SPECTRUM to File ***************/

void dumpTOF()
{
     FILE *dump;
```

```
     char ofnam[80];
     int i;

     do   {
               locate(7,10);
               printf("%50s"," ");
               locate(7,10);
               printf("file name for output?: ");
               skeyin(ofnam);
               dump = fopen(ofnam,"a");
          } while(dump == NULL);
     fprintf(dump,HEADLN);
     for(i=0;i<ebins[0];i++)
          {
               fprintf(dump,"%f %f\n",Massfact*
               (esig[0][0][i]*0.174757+0.4298364)*
               (esig[0][0][i]*0.174757+0.4298364),
               esig[0][1][i]);
          }
     fclose(dump);
}

/*************** Hot-Key Function Calls *****************/

void menu(int cc)
{
     int d,i;
     double temp;

     switch(cc)
     {
          case '0': active=0;break;
          case 'a': vmax=evmax;vmin=evmin;iscale=1.2;break;
          case 'i':in_data(scan);break;
          case 'c': cursor_on^=1;break;
          case 'm':typeout^=1;break;
          case 'M':      locate(6,10);printf("Mass Factor?
               ",Massfact);temp=inf();if(temp>0)
               Massfact=sqrt(temp/((Massfact*cursor*0.174757
               +0.4298364)*(Massfact*cursor*0.174757+0.42983
               64)));
               break;
          case 'O': dumpTOF();break;
          case 'w': black_on_white();break;
          case 'x':locate(6,10);printf("freq minimum
               (%12.11f)?:",vmin);
               temp=inf();if(temp>0) vmin=temp;
               locate(7,10);printf("freq maximum
               (%12.11f)?:",vmax);
```

```
     temp=inf();if(temp>0) vmax=temp;
     break;
case 'y': locate(6,10);printf("vertical scale
     (%6.2lf)?:",iscale);
     temp=inf(); if(temp>0.0) iscale=temp; break;
case 27: c='q';break;
case 0: d=getch();  temp=vmax-vmin;
if(active==0) switch(d)
{
case UpArrow:
     iscale /= 1.2; break;
case DownArrow:
     iscale *= 1.2; break;
case CtrlRightArrow:
     vmin -= (temp/8.0);vmax -= (temp/8.0);break;
case CtrlLeftArrow:
     vmin += (temp/8.0);vmax += (temp/8.0);break;
case AltRightArrow:
     vmin -= (temp/4.0);vmax -= (temp/4.0);break;
case AltLeftArrow:
     vmin += (temp/4.0);vmax += (temp/4.0);break;
case LeftArrow:
     vmax+=(temp/3.0);break;
case RightArrow:
     vmax-=(temp/4.0);break;
case F9:
     cursor -=(temp/256.0);break;
case F10:
     cursor +=(temp/256.0);break;
case ShiftF9:
     cursor -=(temp/64.0);break;
case ShiftF10:
     cursor +=(temp/64.0);break;
case CtrlF9:
     cursor -=(temp/20.0);break;
case CtrlF10:
     cursor +=(temp/20.0);break;
case AltF9:
     cursor -=(temp/3.0);break;
case AltF10:
     cursor +=(temp/3.0);break;
} else switch(d)
{
case UpArrow:
     mult(1.2,1,active-1);break;
case DownArrow:
     mult((1.0/1.2),1,active-1);break;
case CtrlRightArrow:
     shift((temp/128.0),0,active-1);
```

```
                freq_shift[active-1] += (temp/128.0);
                break;
           case CtrlLeftArrow:
                shift((-temp/128.0),0,active-1);
                freq_shift[active-1] -= (temp/128.0);
                break;
           case AltRightArrow:
                shift((temp/64.0),0,active-1);
                freq_shift[active-1] += (temp/64.0);
                break;
           case AltLeftArrow:
                shift((-temp/64.0),0,active-1);
                freq_shift[active-1] -= (temp/64.0);
                break;
           case LeftArrow:
                vmax+=(temp/3.0);break;
           case RightArrow:
                vmax-=(temp/4.0);break;
           case F9:
                cursor -=(temp/256.0);break;
           case F10:
                cursor +=(temp/256.0);break;
           case ShiftF9:
                cursor -=(temp/64.0);break;
           case ShiftF10:
                cursor +=(temp/64.0);break;
           case CtrlF9:
                cursor -=(temp/20.0);break;
           case CtrlF10:
                cursor +=(temp/20.0);break;
           case AltF9:
                cursor -=(temp/3.0);break;
           case AltF10:
                cursor +=(temp/3.0);break;
           }
      break;
      }
}

/***************** Main Control Routine ******************/

int main(int argc, char **argv)
{
      double temp;
      int i;

      vmin=evmin;
      vmax=evmax;
      graphmode();
```

```
    printf(HEADLN);
    for(i=1;i<4;i++) if(argc>i)
         {
         strcpy(fnam[i-1],argv[i]);
         if(!fread_data(fnam[i-1],i-1)) in_data(i-1);
         }
    do
         {
         box();
         plot_esig(0);
         if(ebins[1])plot_esig(1);
         if(ebins[2])plot_esig(2);
         c=getch();
         menu(c);
         } while (c!='q');
    textmode();
    return(0);
}


/******************** End Program TOFMS ******************/
```

1K Program Description

1K is a rotational spectrum simulation program written in the c programming language. The fitting of each band is accomplished through manipulation of the ground and excited state rotational constants as well as the total angular

momentum of the ground state about the bonding axis, Ω'', and the change in total angular momentum upon excitation, $\Delta\Omega$. The relative intensities of the transitions within each band are those given by the Hönl-London factors and the populations of the rotational levels described by a near thermal ensemble. The internal energy distribution used is a composite of two different Boltzmann distributions with different characteristic temperatures, which is typical of ions studied in our apparatus [6,9,10]. The two distributions represent the high J 'tail' resulting from the "freezing in" of rotational energy as the collisional energy drops in the last stages of the supersonic expansion. Convolution of a Gaussian instrument function onto the calculated line-positions results in the contour which is compared directly to the experimental bandshape. In Table A-2, the commands supported by 1K are listed and described.

Table A-2 Commands Supported by Program 1K

Command	Description
S	Baseline Correction
0	Shift Spectrum Up
-	Shift Spectrum Down
O	Write Simulated Contour to File
o	Write Simulated Line Positions to File
m	Decrease Upper-State Centrifugal Distortion Constant
M	Increase Upper-State Centrifugal Distortion Constant

Table A-2 Continued

Command	Description
n	Decrease Lower-State Centrifugal Distortion Constant
N	Increase Lower-State Centrifugal Distortion Constant
K	Increase Lower State Angular Momentum (Spin + Orbit)
k	Decrease Lower State Total Angular Momentum, Ω'',(Spin + Orbit)
P	Toggle Between Perpendicular ($\Delta\Omega = \pm 1$)and Parallel Transition ($\Delta\Omega = 0$)
a	Toggles Automatic Scaling on/off
i	Input Data File
I	Toggles Display of Spectrum on/off
b	Draw Simulated Contour and Stick Spectrum
,	Increment Upper Rotational Constant by a Factor of 5 Times the Current Increment
.	Decrease Upper Rotational Constant by a Factor of 5 Times the Current Increment
<	Increase Vertical Scale of Spectrum
>	Decrease Vertical Scale of Spectrum
c	Toggles Simulated Contour on/off
U	Increase Upper State Rotational Constant
u	Decrease Upper State Rotational Constant
v	Decrease Band Origin
V	Increase Band Origin
w	Change Screen To Black and White Display
L	Increase Lower State Rotational Constant
l	Decrease Lower State Rotational Constant
t	Decrease Temperature
T	Increase Temperature

Table A-2 Continued

Command	Description
r	Brings Up Screen Where Any of the Rotational Constants may be Changed, Calls rot_constants
R	Brings Up Screen Where Any of the Increments of the Rotational Constants, the Resolution of the Contour, and the Number of Rotational Levels may be changed
J	Increase J' of the Marked Transition to be Locked by the Command 'x'
j	Decrease J' of the Marked Transition to be Locked by the Command 'x'
x	Locks the Position of the Peak Selected Using J and j
A	Turns off Automatic Scaling and Reads in New Energy Axis Limits
y	Prompts for Vertical Scaling

1K.c Program Code

```
/*********************************************************/
/********************** Program 1k.c *********************/
/******************* Last Revised 1/12/96 ****************/
/******** Written by and P. J. Brucat & T. W. Hayes  ******/
/*********************************************************/
#define LINT_ARGS
#include <pjb.h>
#include <stdlib.h>
#include <stdio.h>
#define HEADLN "<1K> Spectrum Simulator whole integral J,K
1/12/96 /pjb/twh\n"
#define graphmode()      _setvideomode(16)    /* 640 X 350 */
#define textmode()       _setvideomode(_DEFAULTMODE)
#define cls()            _clearscreen(_GCLEARSCREEN)
#define locate(a,b)      _settextposition(a+1,b+1)
#define HRES             512
#define LEFT             64
#define RIGHT            576
#define TOP              60.0
```

```
#define BOT             290.0
#define TOPBOT          -230.0      /* TOP minus BOT */
#define OVERSIZE        1.2
#define CCUTOFF         1e-5
#define KLOWER          0.0    /*  0.0 normal, 0.5 half
                                   integral */
#define TICKLEN         5.0
#define SNUM            100
#define ESIZE           600
#define ICUTOFF         1e-3
#define TICK_COLOR      15
#define BOX_COLOR       8
#define CURVE_COLOR     14
#define ESIG_COLOR      13
#define BOX_TEXT_COLOR  7
#define P_COLOR         12
#define Q_COLOR         10
#define R_COLOR         9

char            vt[120];
double          startbl,endbl,
          v=15692.33,
          Bup= 0.0655,
          Blow=0.0868,
          Bifact=1.083,
          Dup=1e-100,
          Dlow=1e-100,
          Dinc=1e-7,
          kT=2.0,
          hot_ratio=0.2,
          hot_frac=0.05,qscale=1.0,
          res=0.002,
          lockv,
          targetlock,
          esigmax,
          svmin,svmax,imax,baseline=0,
          cmax,
          vmin,vmax,      /* manual horizontal scaling
factor for plot */
          Binc=0.0001,
          kTinc=1.1,
          iscale=1.2,
          Klower=KLOWER,
          Jmax=30,
          Kmax=8,
          Jlock=(5.0+KLOWER);
char            fnam[80];
int
draw_curve=0,both=0,draw_esig=0,constart=0,conend=0,
```

```
          delJlock=1,
          linelock,
          deltaK=1,
          lock=0,
          dotempto=0,
          start=-1,
          endarray=-1,
          max=1,
          ebins=0,
          dummy=0,
          page=0,
          v_manual=0,
          sticknum=0;     /* running index of sticklist[] */

double far plotdata[HRES],lineshape[HRES];
double far sticklist[3][SNUM];
double far cont_exper[1][HRES];
float far transitions[4][SNUM];
double huge esig[2][ESIZE];

/************ Energy Level Calculation ******************/
double line_frequency(delJ,J)    /*  J=J" */
int delJ;
double J;
{
     double dum;
     dum = v + Bup*(J+delJ)*(J+delJ+1)+Dup*(J+delJ)*
     (J+delJ)*(J+delJ+1)*(J+delJ+1);
     dum -= (Blow*J*(J+1))+Dlow*J*J*(J+1)*(J+1);
     return(dum);
}

/***************** Honl-London Factors ******************/
double HL_fact(delJ,delK,J,K)
int delJ,delK;
double J,K;                      /* J=J"  K=K" */
{
double dum;
switch(delJ)
{
     case 1:
     switch(delK)
               {
               case 0:
               dum = (double)(J+1+K)*(J+1-K)/(J+1);
               break;
               case 1:
                    dum = (double)(J+2+K)*(J+1+K)/(4*(J+1));
                    break;
```

```
                case -1:
                    dum = (double)(J+2-K)*(J+1-K)/(4*(J+1));
                    break;
                }
    break;
    case 0:
        switch(delK)
            {
                case 0:
                    dum (double)(2*J+1)*K*K/
                    (J*(J+1));
                    break;
                case 1:
                    dum =(double)(J+1+K)*(J-K)*(2*J+1)/
                    (4*J*(J+1));
                    break;
                case -1:
                    dum = (double)(J+1-K)*(J+K)*
                    (2*J+1)/(4*J*(J+1));
                    break;
            }
        break;
        case -1:
        switch(delK)
            {
                case 0:
                    dum = (double)(J+K)*(J-K)/J;
                    break;
                case 1:
                    dum = (double)(J-1-K)*(J-K)/(4*J);
                    break;
                case -1:
                    dum = (double)(J-1+K)*(J+K)/(4*J);
                    break;
            }
        break;
    }
return(dum);
}

/************* Vertical Offset of Spectrum****************/
esig_shift(a)
double a;
{
 int i;
    for(i=0;i<ebins;i++)
        esig[1][i] += a;
}
```

```
/*********** Boltzmann Factor for Intensities *************/
double Boltz_fact(J,K)
double J,K;
{
double dum,ret;
     dum = -(Blow*J*(J+1))/kT;
     ret = (1.0-hot_frac)*exp(dum);
     dum = -(Blow*J*(J+1)*hot_ratio)/kT;
     dum = exp(dum);
     dum *= hot_frac;
     ret += dum;
     return(ret);
}

/********** Zero plotdata and sticklist Arrays ************/
clear_plotdata()
{
 int i;
     for(i=0;i<HRES;i++)
          plotdata[i] = 0.0;
     for(i=0;i<SNUM;i++)
               sticklist[0][i] = sticklist[1][i] =
               sticklist[2][i] = 0.0;
     sticknum=0;
}

/**********Array of Line Positions Generated **************/
add_line(vline,iline,delJ,J,delK,Klow)
double vline,iline;
int delJ,delK;
double J,Klow;
{
     sticklist[0][sticknum] = vline;
     sticklist[1][sticknum] = iline;
     switch(delJ)
          {
                    case -1:
               sticklist[2][sticknum] = P_COLOR;
               break;
                    case 0:
               sticklist[2][sticknum] = Q_COLOR;
               break;
                    case 1:
               sticklist[2][sticknum] = R_COLOR;
               break;
          }
     transitions[0][sticknum]=(float far)J;
     transitions[1][sticknum]=(float far)(J+delJ);
     transitions[2][sticknum]=(float far)Klow;
```

```
     transitions[3][sticknum]=(float far)(Klow+delK);
     if((J==Jlock)&&(delJ==delJlock))
          linelock=sticknum;lockv=sticklist[0][sticknum];
     sticknum++;
      if(sticknum>=SNUM)
          {    locate(10,20);
               printf("MEMORY OVERFLOW ...");
               getch();
                    printf("\n\n\t\tYou should exit
                    now");getch();
          }
}

/********** Selection Rules and Calls to Frequency and
Intensity Routines **********/
stick_spectrum()
{
int delJ,delK;
double J,Klow;
double vline,iline;
delK=deltaK;
Klow=Klower;
      if((Klow+delK)>=0)
          for(J=Klow;J<=Jmax;J++)
          for(delJ=-1;delJ<=1;delJ++)
          if((J+delJ)>=(Klow+delK))
          if(delJ || delK || (Klow!=0.0))
               {
                    vline = line_frequency(delJ,J);
                    iline = HL_fact(delJ,delK,J,Klow);
                    iline *= Boltz_fact(J,Klow);
                    if (delJ==0) iline*=qscale;
                    add_line(vline,iline,delJ,J,delK,Klow);
               }
}

/********  Generate Instrument Lineshape Function *********/
gen_lineshape()
{
int i;
double dum,df;
     df = (vmax-vmin)/HRES;
     max =(int)floor(-(res/(df*df))*log(CCUTOFF));
     if(max<1) max=1;
     if(max>HRES) max=HRES;
     for(i=0;i<max;i++)
          {
                    dum = i*df;
                    dum = -(dum*dum)/res;
```

```
                    lineshape[i] = exp(dum);
          }
     for(i=max;i<HRES;i++)
     lineshape[i]=0.0;
}

/********** Contour Array Generation *********************/
add_lineshape(cent,iline)
int cent;
double iline;
{
int j,jj;
     jj=cent+max;
     if(jj>HRES) jj=HRES;
     for(j=cent;j<jj;j++)
          if(j>=0) plotdata[j]+=iline*lineshape[j-cent];
      jj=cent-max;
     if(jj<0) jj=0;
     for(j=cent-1;j>=jj;j--)
          if(j<HRES) plotdata[j]+=iline*lineshape[cent-j];
}

/****************** Contour Calls ***********************/
contour()
{
int i,icent;
double cent,df,p0,p1,dum;
df=(vmax-vmin)/((double)HRES);
for(i=0;i<sticknum;i++)
     {
               dum=(sticklist[0][i]-vmin)/df;
               cent=floor(dum);
               icent=(int)cent;
               p1=dum-cent;
               p0=1.0-p1;
               add_lineshape(icent,p0*sticklist[1][i]);
               add_lineshape((icent+1),p1*sticklist[1][i]);
     }
}

/*********** Finds Maximum of Array plotdata *************/
cscale()
{
int i;
     cmax=plotdata[0];
     for(i=1;i<HRES;i++)
          if(cmax<plotdata[i]) cmax=plotdata[i];
}
```

```
/************ Scales Simulation Intensities **************/
sscale()
{
int st,fl=1;
imax=sticklist[1][0];
for(st=0;st<sticknum;st++)
     imax=(imax<sticklist[1][st])?sticklist[1][st]:imax;
for(st=0;st<sticknum;st++)
     if (sticklist[1][st]>imax*ICUTOFF)
          {
               if(fl)
               {
                    fl=0;
                    svmin=svmax=sticklist[0][st];
               }
                    svmin=(svmin>sticklist[0][st])?sticklist
                    [0][st]:svmin;
                    svmax=(svmax<sticklist[0][st])?sticklist
                    [0][st]:svmax;
          }
     svmax=(0.55)*(svmax-svmin)+(0.5)*(svmax+svmin);
     svmin=(-0.55)*(svmax-svmin)+(0.5)*(svmax+svmin);
}

/************ Experimental Data File Input **************/
fread_esig()
{
FILE *dfile;
double frq,dis;
int i;
     do
          {
               locate(7,10);printf("%50s"," ");
               locate(7,10);printf("Experimental data file
               for input?: ");
               skeyin(fnam);
               dfile = fopen(fnam,"r");
          } while(dfile == NULL);
     for(ebins=0;((fscanf(dfile," %lf %lf\n",&frq,&dis) !=
     EOF) && (ebins<ESIZE));ebins++)
          {    esig[0][ebins]=frq;
               esig[1][ebins]=dis/100;
          }
     fclose(dfile);
     esigmax=esig[1][0];
     for(i=0;i<ebins;i++)
          if (esig[1][i] > esigmax) esigmax=esig[1][i];
}
```

```
/********** Writes Simulation Line List to File  **********/

dump_list()
{
FILE *dumpfile;
char fnam[80];
int i;
double Jup,Jlow,Kup,Klow;
double frq,dss;
     do
          {
                    locate(7,10);printf("%50s"," ");
                    locate(7,10);printf("file for output?:
                    ");
                    skeyin(fnam);
                    dumpfile = fopen(fnam,"a+");
          } while(dumpfile == NULL);
     fprintf(dumpfile,HEADLN);
     fprintf(dumpfile,"\n\n%10s%10s%10s%10s%15s%15s\n",
     "Kupper","Klower","Jupper","Jlower","frequency","intens
     ity");
     for(i=0;i<sticknum;i++)
          {
               Kup=(double)transitions[3][i];
               Klow=(double)transitions[2][i];
               Jup=(double)transitions[1][i];
               Jlow=(double)transitions[0][i];
               fprintf(dumpfile,"\n%10.1lf%10.1lf%10.1lf%10.
               1lf%10.1lf",Kup,
               Klow,Jup,Jlow);
               frq=sticklist[0][i];
               dss=sticklist[1][i];
               fprintf(dumpfile,"%15.2lf%15lf",frq,dss);
          }
     fprintf(dumpfile,"\n\n");
     fclose(dumpfile);
}

/******* Subtracts Baseline of Rotational Spectrum ********/

getbaseline()
{
int i,j;
double temp,total;
     i=0;
     total=0.0;
     locate(7,10);
     printf("\n\t input start of baseline:([%5.2lf])
     ",startbl);
```

```
     if ((temp=inf()) > 0.0)
          startbl = temp;
     printf("\n\t input end of baseline:([%5.2lf])",endbl);
     if ((temp=inf()) > 0.0)
          endbl = temp;
     do {i++;} while (esig[0][i]<startbl);
     j=i;
     do{j++;total+=esig[1][j];} while (esig[0][j]<endbl);
     baseline=total/(j-i);
     for(i=0;i<ebins;i++)
          {
               esig[1][i]-=baseline;
          }
}

/********* Generates Contour Array cont_exper  ************/

Cont_exp_Dump()
{
int i,j,l,nexti,start,endarray;
double maxesig,maxcont;
char a;
double exp_inc,cont_inc;
     cont_inc=(vmax-vmin)/512;
     maxesig=1.0;
     maxcont=1.0;
     for(i=0;i<HRES;i++)
          {
          cont_exper[1][i]=(double)plotdata[i];
          cont_exper[0][i]=(double)vmin+i*cont_inc;
          }
     j=0;
     l=0;
     do {l++;} while (esig[0][l] < cont_exper[0][0]);
     constart=l;
     for(i=constart;i<ebins;i++)
          {
          if (fabs(esig[0][i]-cont_exper[0][j])<0.0001)
          {
          esig[2][i]=cont_exper[1][i];
          }
          else if (esig[0][i]>cont_exper[0][j])
          {
          do {j++;} while (cont_exper[0][j] < esig[0][i]);
          if (cont_exper[0][j]==esig[0][i])
          esig[2][i]=cont_exper[1][j];
          else esig[2][i] =
          ((esig[0][i]-cont_exper[0][j-1])/(cont_exper[0][j]
          -cont_exper[0][j-1]))*(cont_exper[1][j]-
```

```
        cont_exper[1][j-1])+cont_exper[1][j-1];
        }
        else if (esig[0][i]<cont_exper[0][j])
        {
        do {j--;} while (esig[0][i] <
        cont_exper[0][j]);
        if (cont_exper[0][i]== cont_exper[0][j])
        esig[2][i]=cont_exper[1][j];
        else esig[2][i]=((esig[0][i]-cont_exper[0][j])/
        (cont_exper[0][j]-cont_exper[0][j+1]))*
        (cont_exper[1][j+1]-cont_exper[1][j])+
        cont_exper[1][j];
        }
        if (esig[1][i]>(double)maxesig)
        maxesig=esig[1][i];
        if (esig[2][i]>(double)maxcont)
        maxcont=esig[2][i];
        conend=i;
        if (esig[0][i]>=vmax) i=ebins;
        if (j==511) i=ebins;
        }
        for(i=constart;i<=conend;i++)
        esig[2][i]=(esig[2][i])*(maxesig/maxcont);
}

/************ Writes Simulated Contour to File ************/

Makefile()
{
FILE *dumpfile;
char fnam[80];
int i,start,endarray;

     do
          {
               locate(7,10);printf("%50s"," ");
               locate(7,10);printf("file for output?: ");
               skeyin(fnam);
               dumpfile = fopen(fnam,"a+");
          } while(dumpfile == NULL);
     fprintf(dumpfile,"%9s%15s%15s\n","Frequency","Exper
     Int","Contour Int");
     for(i=constart;i<conend;i++)
          fprintf(dumpfile,"\n%10.2lf  %10.3lf
          %12.3lf",esig[0][i],esig[1][i],esig[2][i]);
     fprintf(dumpfile,"\n\n");
     fclose(dumpfile);
}
```

```
/********** Displays Experimental Spectrum **************/
plot_esig()
{
int i,x,y,onscale=0;
double ehscale;
     if(!ebins) return;
     if(esigmax==0.0) return;
     _setcolor(ESIG_COLOR);
     ehscale = (vmax-vmin);
     y = (int)(BOT + TOPBOT*(esig[1][0]/(esigmax*iscale)));
     if (y<TOP) y=TOP;
     if (y>BOT) y=BOT;
     x = (int)(LEFT+ HRES*((esig[0][0]-vmin)/ehscale));
     if ((x>=LEFT)&&(x<HRES+LEFT))
          {
               _moveto(x,y);
               onscale=1;
          }

     for(i=1;i<ebins;i++)
          {
               y = (int)(BOT +
               TOPBOT*((esig[1][i])/(esigmax*iscale)));
               if (y<TOP) y=TOP;
               if (y>BOT) y=BOT;
               x = (int)(LEFT +
               HRES*((esig[0][i]-vmin)/ehscale));
               if((x>=LEFT)&&(x<HRES+LEFT))
                    {
                    if(onscale) _lineto(x,y);
                    else
                         {
                              _moveto(x,y);
                              onscale=1;
                         }
                    }
               else {onscale=0;}
          }
}

/********** Draws Simulated Contour on Screen *************/

plot_curve()
{
int i,x,y;
     if(iscale*cmax==0.0) return;
     _setcolor(CURVE_COLOR);
     y = BOT + TOPBOT*plotdata[0]/(iscale*cmax);
     if (y<TOP) y=TOP;
```

```
     _moveto(LEFT,y);
     for(i=1;i<HRES;i++)
          {
                    y = (int)(BOT +
                    TOPBOT*plotdata[i]/(iscale*cmax));
                    if (y<TOP) y=TOP;
                    _lineto(LEFT+i-1,y);
          }
}


/************* Draws Stickspectrum on Screen **************/
sticker()
{
int i,x,y;
     if(iscale==0.0) return;
     for(i=0;i<sticknum;i++)
          {
          if(i==linelock)
               {if(lock) _setcolor(15);
               else_setcolor(7);}
          else
               _setcolor((int)sticklist[2][i]);
          x= LEFT+(int)((double)HRES*(sticklist[0][i]-vmin)/
          (vmax-vmin));
          y = BOT + TOPBOT*(sticklist[1][i]/imax)/iscale;
          if(y<TOP) y=TOP;
          if ((x>LEFT)&&(x<RIGHT))
               {
                    _moveto(x,BOT);
                    _lineto(x,y);
               }
          }
}

/**** Displays Constants and Header Above Spectrum Box ****/

box_text()
{
     char branch;
     switch(delJlock)
               {
               case  0: branch = 'Q';break;
               case  1: branch = 'R';break;
               case -1: branch = 'P';break;
               }
     _settextcolor(BOX_TEXT_COLOR);
     locate(0,0);sprintf(vt,HEADLN);_outtext(vt);
     locate(1,5);sprintf(vt,"v= %9.2lf",v);_outtext(vt);
```

```
     locate(2,5);sprintf(vt,"Klow=%2.1lf
     delK=%2d",Klower,deltaK);_outtext(vt);
     locate(3,5);
     sprintf(vt,"%c(%2.1lf) =
     %9.2lf",branch,Jlock,lockv);_outtext(vt);
     locate(1,30);sprintf(vt,"B'=%8.4lf",Bup);_outtext(vt);
     locate(2,30);sprintf(vt,"B\"=%8.4lf",Blow);_outtext(vt)
     ;
     locate(1,48);sprintf(vt,"D\"=%10.2le",Dlow);_outtext(vt
     );
     locate(2,48);sprintf(vt,"D'=%10.2le",Dup);_outtext(vt);
     if(!v_manual){locate(23,12);sprintf(vt,"auto
     scale");_outtext(vt);}
     if(lock){locate(22,12);sprintf(vt,"line
     lock");_outtext(vt);}
     locate(3,30);
     sprintf(vt,"kT=%4.1lf &
     %4.1lf",kT,kT/hot_ratio);_outtext(vt);
     locate(3,48);sprintf(vt,"file: %s",fnam);_outtext(vt);
     locate(21,3);sprintf(vt,"%7.0lf",vmin);_outtext(vt);
     locate(21,68);sprintf(vt,"%7.0lf",vmax);_outtext(vt);
}

/***** Draws Spectrum Box and Tick Marks *****************/

box()
{
int xt,tick,low,yt,high;
     low = (int)vmin;
     if((double)low<vmin) low++;
     high = (int)vmax;
     if((double)high>vmax) high--;
     _setcolor(BOX_COLOR);
     _moveto(LEFT,(int)BOT);
     _lineto(LEFT,(int)TOP);
     _lineto(RIGHT,(int)TOP);
     _lineto(RIGHT,(int)BOT);
     _lineto(LEFT,(int)BOT);
     _setcolor(TICK_COLOR);
     xt = LEFT+(int)(HRES*(v-vmin)/(vmax-vmin));
     _moveto(xt,BOT+3*TICKLEN);
     _lineto(xt,BOT);
     _moveto(xt+1,BOT+3*TICKLEN);
     _lineto(xt+1,BOT+2*TICKLEN);
     _moveto(xt-1,BOT+3*TICKLEN);
     _lineto(xt-1,BOT+2*TICKLEN);
     for(tick=low;tick<=high;tick++)
               {
               xt = LEFT+(int)(HRES*((double)tick-vmin)/
```

```
                (vmax-vmin));
                _moveto(xt,(int)BOT);
                if(!(tick%10)) yt=BOT+2*TICKLEN;
                else yt=BOT+TICKLEN;
                if(!(tick%2)||((vmax-vmin)<50.0))
                {_lineto(xt,yt);}              }
     box_text();
}

/********** Changes Screen to Black and White ***********/

black_on_white()
{
int i;
     for(i=1;i<16;i++)
          _remappalette(i, _BLACK);
     _remappalette(0,_BRIGHTWHITE);
}

/********* Gets Rotational Simulation Information *********/

rot_constants()
{
double temp;
     locate(6,10);
     printf("\n\tinput band origin[%5lf cm^-1]: ",v);
     if ((temp=inf()) > 0.0) v = temp;
     printf("\n\tinput B\" [%10.6lf cm^-1]: ",Blow);
     if ((temp=inf()) > 0.0) Blow = temp;
     printf("\n\tinput B' [%10.6lf cm^-1]: ",Bup);
     if ((temp=inf()) > 0.0) Bup = temp;
     printf("\n\tinput D\" [%10.2le cm^-1]: ",Dlow);
     if ((temp=inf()) > 0.0) Dlow = temp;
     printf("\n\tinput D' [%10.2le cm^-1]: ",Dup);
     if ((temp=inf()) > 0.0) Dup = temp;
     printf("\n\tinput rotational energy kT [%6.2lf cm^-1]:
     ",kT);
     if ((temp=inf()) > 0.0) kT = temp;
     printf("\n\tinput fraction of 'hot' molecules[%6.3lf]:
     ",hot_frac);
     temp=inf();
     if ((temp > 0.0)&&(temp<1.0)) hot_frac=temp;
     printf("\n\tinput hot/normal temperature ratio[%6.1lf]:
     ",1.0/hot_ratio);
     if ((temp=inf()) > 0.0) hot_ratio=1.0/temp;
}

/********* Gets Rotational Simulation Preferences *********/
```

```
increments()
{
double temp;
       locate(6,10);
     printf("\n\tinstrument resolution squared[%8.4lf
     cm^-1]: ",res);
     if ((temp=inf()) != 0) {res = temp;gen_lineshape();}
     printf("\n\tincrement for B rotational constants
     [%8.4le cm^-1]: ",Binc);
     if ((temp=inf()) != 0) Binc=temp;
     printf("\n\tincrement for D rotational constants
     [%8.4le cm^-1]: ",Dinc);
     if ((temp=inf()) != 0) Dinc=temp;
     printf("\n\tmaximum J to be calculated [%5d]: ",Jmax);
     if ((temp=inf()) != 0) Jmax=(int)temp;
     printf("\n\tQ branch scale factor [%5d]: ",qscale);
     if ((temp=inf()) != 0) qscale=(int)temp;
}

/******** Functions Calls to Supported Commands **********/

menu(c)
char c;
{
char d;
double temp;
     switch(c)
          {
               case 'S':
               getbaseline();break;
               case '+':
               esig_shift(esigmax*iscale/8.0);break;
               case '-':
               esig_shift(-esigmax*iscale/8.0);break;
               case 'O':
               Cont_exp_Dump();Makefile();break;
               case 'm':
               Dup-=Dinc;break;
               case 'M':
               Dup+=Dinc;break;
               case 'n':
               Dlow-=Dinc;break;
               case 'N':
               Dlow+=Dinc;break;
               case 'K':
               Klower++; break;
               case 'k':
               Klower--; if(Klower<0) Klower=KLOWER;
               if((deltaK+Klower)<0) Klower = KLOWER-deltaK;
```

```
break;
case 'P':
deltaK--;
if(deltaK<-1) deltaK=1;
if(Klower+deltaK<0) Klower=KLOWER-deltaK;
break;
case 'a':
v_manual^=1;break;
case 'i':
draw_esig=1;fread_esig();break;
case 'I':
draw_esig^=1;break;
case 'o':
dump_list();break;
case 'b':
both^=1;break;
case ',':
Bup+=5.0*Binc;Blow+=5.0*Binc;break;
case '.':
Bup-=5.0*Binc;Blow-=5.0*Binc;
if(Bup<=0.0) Bup=Binc; if(Blow<=0.0)
Blow=Binc;break;
case '<':
esigmax *= 1.2;break;
case '>':
esigmax /= 1.2;break;
case 'c':
draw_curve^=1; break;
case 'U':
Bup+=Binc; break;
case 'u':
Bup-=Binc; if(Bup<=0.0) Bup=Binc; break;
case 'v':
v-=(vmax-vmin)/64.0; break;
case 'V':
v+=(vmax-vmin)/64.0; break;
case 'w':
black_on_white();break;
case 'L':
Blow+=Binc; break;
case 'l':
Blow-=Binc; if(Blow<=0.0) Blow=Binc; break;
case 'T':
kT*=kTinc;break;
case 't':
kT/=kTinc;break;
case 'r':
rot_constants();break;
case 'R':
```

```
                increments();break;
                case 'J':
                delJlock++;if(delJlock>1){delJlock=-1;Jlock++
                ;}break;
                case 'j':
                delJlock--;if(delJlock<-1){delJlock=1;Jlock--
                ;}break;
                case 'x':
                lock^=1;if(lock)targetlock=lockv;break;
                case 'A':
                v_manual=1;
                locate(6,10);
                printf("lower frequency limit (%12.21f)?:
                ",vmin);
                if ((temp=inf()) != 0) vmin = temp;
                locate(7,10);
                printf("upper frequency limit (%12.21f)?:
                ",vmax);
                if ((temp=inf()) != 0) vmax = temp;
                gen_lineshape();break;
                case 'y':
                locate(6,10);
                printf("vertical scale (%6.2lf)?:",iscale);
                temp=inf();
                if(temp>0.0) iscale=temp; break;
        }
}

/************ Controls all Screen Updates *****************/

spec_display()
{
     clear_plotdata();
     stick_spectrum();
     if(lock)
                {
                v-=(lockv-targetlock);
                clear_plotdata();
                stick_spectrum();
                }
     sscale();
     if(!v_manual)
          {
                vmin=svmin; vmax=svmax;
                gen_lineshape();
                iscale=1.2;
          }
     page ^=1;
     _setactivepage(page);
```

```
     cls();
     box();
     if(draw_esig) plot_esig();
     if(draw_curve)
               {
               contour();
               cscale();
               plot_curve();
               if(both) sticker();
               }
     else sticker();
     _setvisualpage(page);
}

/************ Main Control Routine ************************/

main()
{
char c;
     graphmode();
     printf(HEADLN);
     menu('c');
     do
          {
               spec_display();
               while (kbhit()) getch();
               c=getch();
               menu(c);
          } while (c!='q');
     textmode();
}
/************ End Program 1K ************************/
```

LIST OF REFERENCES

1. G. Herzberg, *Spectra of Diatomic Molecules*, (Van Nostrand Reinhold Co., New York, 1950).

2. J. O. Hirschfelder, C. F. Curtiss and R. B. Bird, *Molecular Theory of Gases and Liquids*, (Joun Wiley, New York, 1964).

3. D. H. Levy, *Ann. Rev. Phys. Chem.*, **31**, 197 (1980).

4. T. Buthelezi, D. Bellert, V. Lewis, K. Dezfulian, J.Kisko, T. Hayes and P. J. Brucat, *Chem. Phys. Lett.*, **257**, 340 (1996).

5. R. L. Asher, D. Bellert, T. Buthelezi and P.J. Brucat, *Chem Phys. Lett.*, **228**, 599 (1994).

6. R. L. Asher, D. Bellert, T. Buthelezi and P. J. Brucat, *Chem Phys. Lett.*, **227**, 277 (1994).

7. D. Lessen and P. J. Brucat, *J. Chem. Phys*, **90**, 6296 (1989).

8. D. Bellert, T. Buthelezi, V. Lewis, K. Dezfulian, D. Reed, T. Hayes and P. J. Brucat, *Chem. Phys. Lett.*,**256**, 555 (1996).

9. T. Buthelezi, D. Bellert, V. Lewis and P. J. Brucat, *Chem. Phys. Lett.*, **242**, 627 (1995).

10. R. L. Asher, D. Bellert, T. Buthelezi, Dan Lessen and P. J. Brucat, *Chem. Phys. Lett.*, **234**, 119 (1995).

11. K. C. Smyth and P. K. Schenck, *Chem. Phys. Lett.*, **55**, 466 (1978).

12. J. K. Nestor, *Applied Optics*, **21**, 4154 (1982).

13. W. Demtroder, *Laser Spectroscopy, Basic Concepts and Instrumentation, Chemical Physics 5*, (Springer-Verlag, 3rd ed., New York, 1988).

14. B. S. Freiser, *Organometallic Ion Chemistry*, (Kluwer Academic Publishers, 1996).

15. A. W. Castleman, Jr. and R. G. Keesee, *Chem Rev.*, **86**, 589, (1986).

16. E. E. Ferguson, *Annu. Rev. Phys. Chem.*, **26**, 17 (1975).

17. F. A. Khan, D. L. Steele and P. B. Armentrout, *J. Phys. Chem.*, **99**, 7819, (1995).

18. R. H. Schultz, K. C. Crellin and P. B. Armentrout, *J. Am. Chem. Soc.*, **113**, 8590, (1991).

19. S. Loh, L. Li and P. B. Armentrout, *J. Am. Chem. Soc.*, **111**, 3167, (1989).

20. N. Aristov and P. B. Armentrout, *J. Phys. Chem.*, **90**, 5135 (1986).

21. P. R. Kemper, M. Hsu, M. T. Bowers, *J. Phys. Chem.*, **95**, 10600, (1991).

22. J. E. Maitre, P. R. Kemper, M. T. Bowers, *J. Chem Phys.*, **106**, 10153, (1997).

23. J. W. Coburen, E. Taglauer, E. Kay, *J. Appl. Phys.*, **45**, 1779 (1974).

24. C. R. Aita, T. A. Myers and W. J. LaRocca, *J. Vac. Sci. Technol.*, **18**, 324, (1981).

25. L. B. Knight, Jr., *Acc. Chem. Res.*, **19**, 313, (1986).

26. R. J. Van Zee and W. Weltner, Jr., *J. Chem. Phys.*, **89**, 4444, (1988).

27. D. Lessen and P. J. Brucat, *J. Chem. Phys.*, **91**, 4522, (1989).

28. T. Buthelezi, D. Bellert, T. Hayes and P. J. Brucat, *Chem. Phys. Lett.*, **262**, 303, 1996.

29. D. Bellert, T. Buthelezi, T. Hayes and P. J. Brucat, *Chem. Phys. Lett.*, **260**, 458 (1996).

30. D. Bellert, T. Buthelezi, T. Hayes and P. J. Brucat, Accepted *Chem. Phys. Lett.*, July 1997.

31. C. E. Moore, Natl. Bur. Stand. Circ. (US) 467 (1952).

32. J. LeRoy and R. B. Bernstein., *J. Mol. Spectrosc.*, **37**, 109, (1971).

33. R. L. Asher, D. Bellert, T. Buthelezi, V. Lewis, and P. J. Brucat. *Chem. Phys. Lett.*, **234**, 113, (1995).

34. J. F. Bottcher and P. Bordewijk, *Theory of Electric Polarization, Vol. II*, (Elsevier, Amsterdam, 1978).

35. H. Partridge, C. W. Bauschlicher Jr, *J. Phys. Chem.*, **98**, 2301 (1994).

36. T. Bastug, W. D. Sepp, B. Fricke, E. Johnson and C. M. Barshick, *Phys. Rev. A*, **52**, 2734, (1995).

37. B. L. Hammond, W. A. Lester, Jr., M. Braga and C.A. Taft, *Phys. Rev. B*, **41**, 10447 (1990).

38. P. M. Morse, *Phys. Rev.*, **34**, 57 (1929).

39. A. Kratzer, *Zeit. F. Physik.*, **3**, 289 (1920).

40. C. L. Pekeris, *Phys. Rev.*, **45**, 98 (1934).

41. M. Born and J. E. Mayer, *Z. Physik*, **75**, 1 (1932).

42. S. E. Koonin, D. C. Meredith, Computational Phusics (Addison-Wesley, New York, 1990).

43. University of Waterloo Chemical Physics Research Report CP-555R (1996).

44. C. W. Bauschlicher, Jr., H. Partridge and S. R. Langhoff, *Chem. Phys. Lett.*, **165**, 272, (1990).

45. R. L. Asher, D. Bellert, T. Buthelezi and P. J. Brucat, *Chem. Phys. Lett.*, **224**, 525 (1994).

46. C. Luder, M. Velegrakis, *J. Chem. Phys.*, **105**, 2167, (1996).

47. D. E. Lessen, R. L. Asher, P. J. Brucat, *Chem. Phys. Lett.*, **177**, 380 (1991).

48. C. Heinemann, J. Schwarz, Wolfram Koch, H. Schwartz, J. *Chem. Phys.*, **103**, 4551, (1995).

49. C. Berg, T. Schindler, G. Niedner-Schatteburg, V. E. Bondybey, *J. Chem. Phys.* **102**, 4870 (1995).

50. N. Aristov, P. B. Armentrout, *J. Phys. Chem.* **91**, 6178 (1987).

51. R. H. Schultz, P. B. Armentrout, *J. Phys. Chem.* **97**, 596 (1993).

52. P. R. Kemper, J. Bushnell, P. van Koppen, M. T. Bowers, *J. Phys. Chem.* **97**,1810 (1993).

53. C. L. Haynes, P. B. Armentrout, J. K. Perry, W. A. Goddard III, *J. Phys. Chem.* **99**, 6340 (1995).

54. Y. C. Cheng, J. Chen, L. N. Ding, T. H. Wong, P. D. Kleiber, *J. Chem. Phys.* **104**, 6452 (1996).

55. Lessen, R. L. Asher, P. J. Brucat, *J. Chem. Phys.* **93**, 6102 (1990).

56. M. R.Blomberg, P. E. M. Siebahn, M. Svensson, *J. Phys. Chem.* **98**, 2062 (1994).

57. A. Fiedler, D. Schroder, S. Shaik, H. Schwarz, *J. Am. Chem. soc.* **116**, 10734 (1994).

58. A. Fiedler, J. Hrusak, W. Koch, H. Schwarz, *Chem. Phys. Lett.* **211**, 242 (1993).

59. H. Kang, J. L. Beauchamp, *J. Am. Chem. Soc.* **108**, 5663 (1986).

60. M. Sodupe, V. Branchadell, M. Rosi, C. W. Bauschlicher, Jr. submitted to *J. Chem. Phys.*

61. E. Carter, W. Goddard, III, *J. Phys. Chem.* **92**, 2109, (1988).

62. A. G. Adam, Y. Azuma, J. Barry, G. Huang, M. Lyne, A. Merer, J. Schroder, *J. Chem. Phys.* **86**, 5231 (1987).

63. E. Bakalbassis, M. Stiakaki, A. Tsipis, C. Tsipis, *Chem. Phys.* **205**, 389 (1996).

64. A. J. Merer, *Annu. Rev. Phys. Chem.* **40**, 407 (1989).

65. D. E. Lessen, Spectroscopic Characterization of Novel Cluster Ions, Ph.D. Dissertation, University of Florida, Gainesville (1992).

BIOGRAPHICAL SKETCH

Thomas W. Hayes was born April 18, 1969, to James and Susan Hayes in Hartfort, Connecticut. In 1969 his family moved to Fairport, New York where he attended K-12th grade. Following graduation from Fairport High School in 1987, he attended the College of Wooster, located in Wooster, Ohio, where he earned a Bachelor of Arts Degree in 1992, with a major in chemistry. From the Fall of 1992 through 1997, he attended the University of Florida where he earned his PhD. in Physical Chemistry under the Direction of Dr. Philip J. Brucat. The author's research focused on the interpretation of the vibrational and rotational photodissociation spectra of transition metal cationic complexes.

I certify that I have read this study and that in my opinion it conforms to acceptable standards of scholarly presentation and is fully adequate, in scope and quality, as a dissertation for the degree of Doctor of Philosophy.

Philip J. Brucat, Chair
Associate Professor of
Chemistry

I certify that I have read this study and that in my opinion it conforms to acceptable standards of scholarly presentation and is fully adequate, in scope and quality, as a dissertation for the degree of Doctor of Philosophy.

William Weltner, Jr
Professor of Chemistry

I certify that I have read this study and that in my opinion it conforms to acceptable standards of scholarly presentation and is fully adequate, in scope and quality, as a dissertation for the degree of Doctor of Philosophy.

David E. Richardson
Professor of Chemistry

I certify that I have read this study and that in my opinion it conforms to acceptable standards of scholarly presentation and is fully adequate, in scope and quality, as a dissertation for the degree of Doctor of Philosophy.

Yngve Öhrn
Professor of Chemistry

I certify that I have read this study and that in my opinion it conforms to acceptable standards of scholarly presentation and is fully adequate, in scope and quality, as a dissertation for the degree of Doctor of Philosophy.

Alex Green
Graduate Research Professor
Mechanical Engineering

This dissertation was submitted to the Graduate Faculty of the Department of Chemistry in the College of Liberal Arts and Sciences and to the Graduate School and was accepted as partial fulfillment of the requirements for the degree of Doctor of Philosophy.

December, 1997

_____

Dean, Graduate School